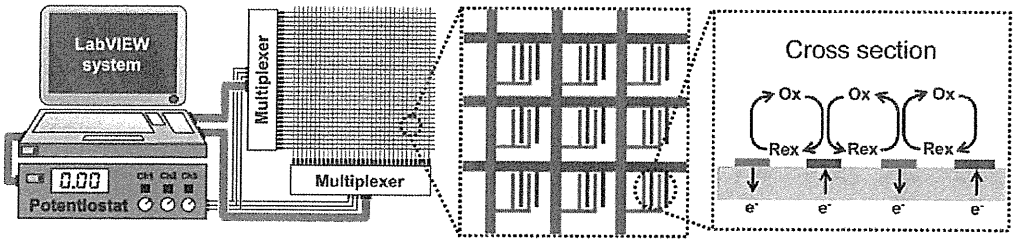

Fig. 1 Schematic illustration of local redox cycling-based electrochemical detection. The device consists of 32 column and 32 row electrodes. The column electrodes are perpendicular to the row electrodes and an IDA is fabricated in each microwell located at the individual crossing points. A potentiostat is connected to these electrodes through a multiplexer and the instruments are controlled with a computer. Local redox cycling is induced only at the IDAs located at designated cross points. Red and blue electrodes indicate column and row electrodes, respectively.

S1a†). A row electrode was connected to one comb-type electrode of the IDA. The row electrodes were insulated with SU-8 (thickness, 2 μm) (Fig. 2b and S1b†) for separation of the row and column electrodes and then Ti/Pt was sputtered on the substrates to fabricate a column electrode connected to the other comb-type electrode of the IDA (Fig. 2c and S1c†). Finally, the column electrodes were insulated with SU-8 (thickness, 5 μm) to fabricate arrays of measurement microwells with exposed IDAs (Fig. 2d and S1d†). The device consisted of 32 row electrodes and 32 column electrodes to form 1024 sensor points with microwells (length: 100 μm, width: 100 μm, height: 7 μm) (Fig. 2). Each individual IDA can function as an independent electrochemical sensor, and 1024 sensor microwells were incorporated into a small area (approximately 40 mm^2) (Fig. 2e). The images of the IDAs show that the width of each electrode finger and the gap between the fingers are approximately 8 and 12 μm, respectively (Fig. 2g and h). Unlike the previous assembly, the present device has the row/column electrodes and resulting sensor wells placed on a single substrate. Since the sensor well with IDA has a wide opening, a sample solution containing analyte materials can easily be introduced into the device and recovered after the measurement.

Clip connectors (CCNL-050-37-FRC, Yokowo, Tokyo, Japan) were connected to the device for multipoint electrochemical detection (ESI, Fig. S2†). The clip connectors were installed to multiplexers (NI

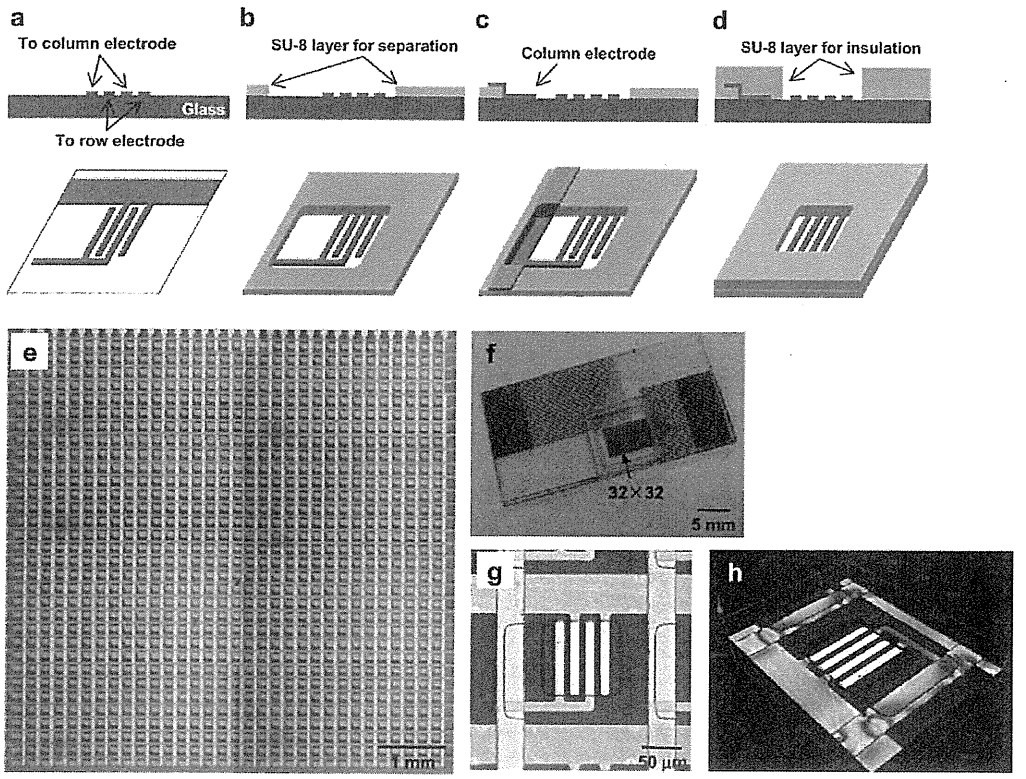

Fig. 2 (a–d) Schematic illustration of the device fabrication process. (a) Ti/Pt is sputtered on a glass substrate to fabricate the row electrodes and IDAs. (b) The insulation layer (SU-8) is fabricated on the substrate to separate the row and column electrodes. (c) Ti/Pt is sputtered on the substrate to form the column electrodes. (d) A second SU-8 layer insulates the sensor microwells. Images of (e and f) the 32 × 32 crossing points, and (g and h) the sensor point. An acrylic frame was placed on the device for keeping sample solutions on the sensor points (f).

PXI-2529, National Instruments, Austin, TX) and a multichannel potentiostat (HA-1010 mM4, Hokuto Denko, Tokyo, Japan) to control the voltage applied to the electrodes. Voltage control and data collection were performed using an AD/DA converter (PXI-6723, National Instruments) through a program written with LabVIEW. Sample solution was introduced onto the device, and an Ag/AgCl reference electrode and a Pt counter electrode were inserted into the sample solution (ESI, Fig. S2†).

Ferrocenemethanol (FMA), a redox compound showing reversible electrochemical behavior, was used to evaluate the device. Fig. 3a shows the amperograms of 4.0 mM FMA in a buffer solution (0.1 M KCl, 25 mM KH_2PO_4 and 25 mM Na_2HPO_4) at a sensor point. The oxidation current at the column electrode was divided by 32 to calculate the current based on redox cycling at a single sensor point. The amperograms at the column electrode (generator) show a transient spike upon the potential step from 0.00 to 0.50 V and then reach a steady-state current for oxidation of FMA. The reduction current at the row electrode (collector) set at 0.00 V increased immediately at the potential step and reached a steady-state, which indicates that FMA^+ generated at the column electrode was reduced at the row electrode. The collection efficiency (the ratio of reduction current at the row electrode to oxidation current at the column electrode at steady-state) was found to be approximately 50% (Fig. 3a). The electrochemical response reached a steady state within 1000 ms after the potential step (Fig. 3a), so the period for precondition was set at 1000 ms (ESI, Fig. S3†). The electrochemical signals at the individual sensors were proportional to the concentration of FMA (Fig. 3b). *p*-Aminophenol (*p*AP), a redox compound showing reversible electrochemical behavior, was also detected, and concentration-dependent electrochemical signals were acquired.

The scanning process was automatically performed using a program written with LabVIEW, as described in our previous paper[8] and Fig. S3†. Electrochemical responses at the 1024 sensors were collected by sequentially changing the potential applied to the column and row electrodes, allowing the system to be addressable within 1 min (ESI, Fig. S3†). As a demonstration of multipoint addressable electrochemical detection, designated sensor microwells were coated with bovine serum albumin (BSA) membrane. A mixture of 1.0 mg BSA, 15 mL of water, and 2 mL of 5% glutaraldehyde (GA) was prepared and dropped onto some of the sensor microwells. The character "ON" was drawn on the device with the BSA mixture, and the FMA solution was then introduced into the device. After adding the FMA solution, the electrochemical signals at the individual sensors were acquired. The BSA membranes blocked the redox cycling of FMA/FMA^+, so the electrochemical responses at the designated microwells were significantly decreased compared with the uncoated microwells (Fig. 3c). These results show that the device can be applied to multipoint addressable electrochemical detection. Fig. 3c also shows that the redox component diffusion between the sensor wells was slight during measurements since the current at the

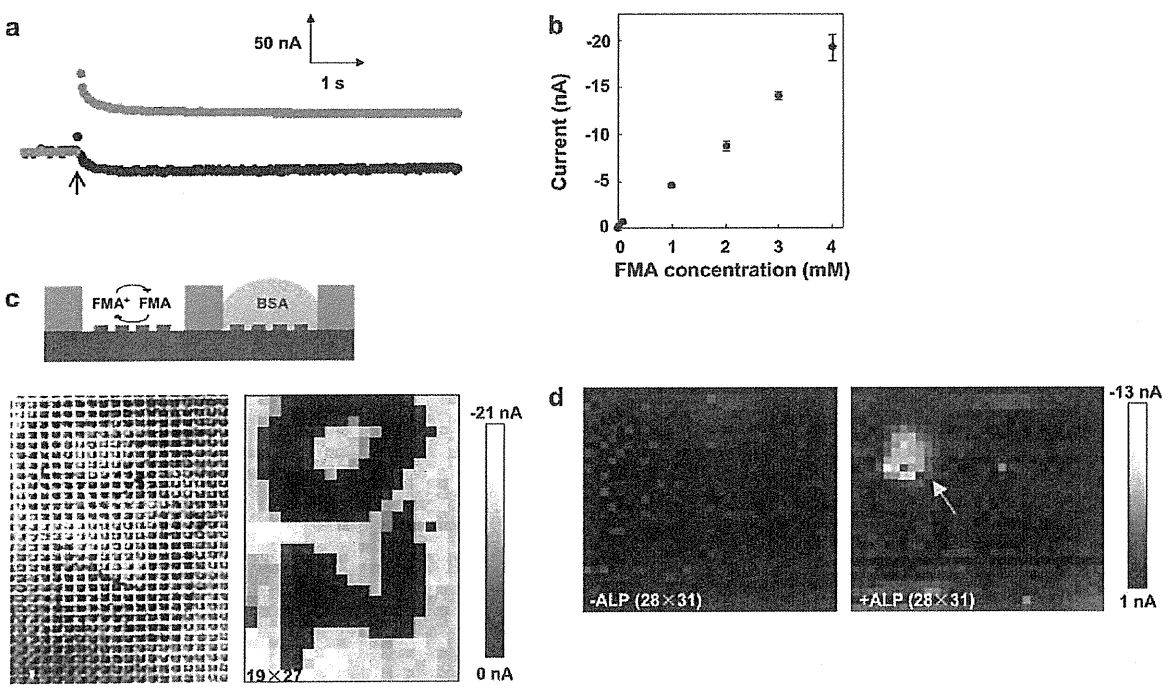

Fig. 3 (a) Amperograms of 4.0 mM FMA observed at the device. Responses from the oxidation of FMA and the reduction of FMA^+ obtained at the column electrode (generator electrode, gray symbol) and row electrode (collector electrode, black symbol), respectively. The column electrode was stepped from 0.00 to 0.50 V at the time indicated by the arrow, while the row electrode was held at 0.00 V. (b) Dependence of the electrochemical signals on the FMA concentration (0.01–4 mM). The signal was detected at the row electrodes 1 s after the potential step of the column electrodes from 0.00 to 0.50 V. Data points represent the mean ± SD of four-six independent experiments. (c) Schematic illustration showing the blocking effect of BSA membrane on the redox cycling of FMA/FMA^+. Microscopic imaging (bottom left) and electrochemical imaging (19 × 27 pixels) (bottom right) of the device showing the character "ON". BSA membranes efficiently blocked the redox cycling. (d) Electrochemical imaging (28 × 31 pixels) of ALP. Although no electrochemical responses were acquired before adding ALP/BSA aggregate (left image), the electrochemical response indicated by the arrow was acquired after adding the ALP/BSA aggregate (approximately 1 mm diameter) (right image).

first measurement point was similar to the current at the end measurement point.

For electrochemical imaging of enzyme, ALP and *p*APP were used. *p*APP (4.0 mM) in pH 9.0 HEPES buffer solution was introduced into the device. A mixture of 0.2 mg ALP, 1.0 mg BSA, 15 mL water, and 2 mL 5% GA was prepared, and a small amount of the mixture was added into the *p*APP solution with a syringe to make an ALP/BSA aggregate and float the aggregate on the solution. After adding the aggregate, the electrochemical signals at the individual sensors were acquired. The detection scheme for ALP is detailed in Fig. S4†. Briefly, ALP catalyzes the hydrolysis of *p*APP to yield *p*AP, which induces redox cycling,[7–10] similar to that for FMA, and provides an electrochemical image. This redox cycling between the anode and cathode amplifies the electrochemical signal from *p*AP produced by ALP. The image followed the position of the ALP/BSA aggregate in the solution and the intensity was dependent on the ALP activity of the aggregate (Fig. 3d). After moving the ALP/BSA aggregate, the electrochemical signals from ALP were also moved. Enzymes, such as ALP, were successfully detected using the device; therefore, this device could be used as a comprehensive, high-throughput lab-on-a-chip tool for applications such as enzyme-linked immunosorbent assay (ELISA), reporter gene assay for monitoring gene expressions, DNA analysis, and cell culture array. Although an application of electrochemical potentials to electrodes may be a critical issue for adhesive cells, it is unnecessary to bound cells on the electrodes of the device since the device has microwells that can trap cells or spheroids on the sensors for cell assays.

In conclusion, a multipoint addressable electrochemical device with a high density of sensor points was proposed. 32 row and 32 column electrodes were incorporated into the device. An IDA was fabricated in each microwell located at each of the crossing points of the row and column electrodes, which resulted in the formation of 1024 addressable sensor microwells with IDA. Electrochemical signals based on redox cycling from each of the 1024 sensors could be acquired within 1 min. This device has a wide variety of potential applications, including two-dimensional imaging of the distributions of electrochemical species. Enzymes, such as ALP, were successfully detected using the device; therefore, this device could be used as a comprehensive, high-throughput lab-on-a-chip tool for applications such as enzyme-linked immunosorbent assay (ELISA), reporter gene assay for monitoring gene expressions, and DNA analysis.

Acknowledgements

This study was supported by the Formation of Innovation Center for Fusion of Advanced Technologies, Special Coordination Funds for Promoting Science and Technology from the Ministry of Education, Culture, Sports, Science and Technology (MEXT), Japan and also by a Grant-in-Aid for Scientific Research (No. 22245011) from MEXT. This study was also supported by the Casio Science Promotion Foundation.

References

1 K. C. Cheung, P. Renaud, H. Tanila and K. Djupsund, *Biosens. Bioelectron.*, 2007, **22**, 1783–1790.
2 X. Xu, S. Zhang, H. Chen and J. Kong, *Talanta*, 2009, **80**, 8–18.
3 K. Dill, D. D. Montgomery, A. L. Ghindilis, K. R. Schwarzkopf, S. R. Ragsdale and A. V. Oleinikov, *Biosens. Bioelectron.*, 2004, **20**, 736–742.
4 J. H. Pei, M. L. Tercier-Waeber, J. Buffle, G. C. Fiaccabrino and M. Koudelka-Hep, *Anal. Chem.*, 2001, **73**, 2273–2281.
5 Z. Y. Lin, K. Ino, H. Shiku and T. Matsue, *Chem. Commun.*, 2010, **46**, 559–561.
6 Z. Y. Lin, K. Ino, H. Shiku, T. Matsue and G. N. Chen, *Chem. Commun.*, 2010, **46**, 243–245.
7 Z. Y. Lin, Y. Takahashi, T. Murata, M. Takeda, K. Ino, H. Shiku and T. Matsue, *Angew. Chem., Int. Ed.*, 2009, **48**, 2044–2046.
8 Z. Lin, Y. Takahashi, Y. Kitagawa, T. Umemura, H. Shiku and T. Matsue, *Anal. Chem.*, 2008, **80**, 6830–6833.
9 O. Niwa, Y. Xu, H. B. Halsall and W. R. Heineman, *Anal. Chem.*, 1993, **65**, 1559–1563.
10 B. Elsholz, R. Wörl, L. Blohm, J. Albers, H. Feucht, T. Grunwald, B. Jürgen, T. Schweder and B. Hintsche, *Anal. Chem.*, 2006, **78**, 4794–4802.

Biosensors and Bioelectronics 30 (2011) 100–106

Contents lists available at SciVerse ScienceDirect

Biosensors and Bioelectronics

journal homepage: www.elsevier.com/locate/bios

Monitoring oxygen consumption of single mouse embryos using an integrated electrochemical microdevice

Yasumoto Date[a,b], Shinichiro Takano[a], Hitoshi Shiku[a,*], Kosuke Ino[a], Takahiro Ito-Sasaki[c], Masaki Yokoo[d], Hiroyuki Abe[e], Tomokazu Matsue[a,f,**]

[a] Graduate School of Environmental Studies, Tohoku University, Aramaki Aoba 6-6-11, Sendai 980-8579, Japan
[b] Central Research Institute of Electric Power Industry, Abiko 270-1194, Japan
[c] CLINO Co. Ltd., Sendai 980-8574, Japan
[d] Faculty of Bioresource Sciences, Akita Prefectural University, Minami-Akita 010-0444, Japan
[e] Graduate School of Science and Engineering, Yamagata University, Yonezawa 992-8510, Japan
[f] WPI Advanced Institute for Materials Research, Tohoku University, Sendai 980-8577, Japan

ARTICLE INFO

Article history:
Received 6 July 2011
Received in revised form 26 August 2011
Accepted 26 August 2011
Available online 6 September 2011

Keywords:
Embryo
Electrochemical device
Respiration activity
Micro-TAS

ABSTRACT

Oxygen consumption (respiration activity) has been found to be the most remarkable criterion for determining the viability of an embryo produced in vitro. In this study, we propose an accurate, simple, and user-friendly device for measurement of the oxygen consumption of single mammalian embryos. An integrated electrode array was fabricated to determine the oxygen consumption of a single embryo, including the blastocyst stage, which has an inhomogeneous oxygen consumption rate, using a single measurement procedure. A single mouse embryo was positioned in a microwell at the center of an integrated electrode array, using a mouthpiece pipette, and immobilized by a cylindrical micropit with good reproducibility. The oxygen consumption of two-cell, morula, and blastocyst stages was measured amperometrically using the device. The recorded current profile was corrected to take into consideration transient background current during the measurement. A calculation method for oxygen consumption based on spherical diffusion centered on the defined point of the device was developed. This procedure is quite simple because it is not necessary to estimate the radius of the embryo being measured. The calculated values of oxygen consumption for two-cell, morula, and blastocyst stages were $1.36 \pm 0.33 \times 10^{-15}$ mol s^{-1}, $1.38 \pm 0.58 \times 10^{-15}$ mol s^{-1}, and $3.44 \pm 2.07 \times 10^{-15}$ mol s^{-1}, respectively. The increasing pattern of oxygen consumption from morula to blastocyst agreed well with measurements obtained using conventional scanning electrochemical microscopy (SECM).

1. Introduction

Tremendous advances have been witnessed in in-vitro embryo production technologies, such as in vitro maturation, in vitro fertilization, and embryo development. These techniques are key to the production of high quality embryos for biomedical and agricultural applications, such as embryo transfer, cloning, and gene manipulation. Evaluation of embryos produced in vitro is important because the classification of embryo quality allows the optimization of the number of transferred embryos, thus reducing financial losses to animal embryo transfer units, as well as avoiding a large number of unsuccessful and multiple pregnancies in clinics. Moreover, single blastocyst transfer, which follows in vitro fertilization, has received considerable attention in clinical applications because of the high pregnancy rate, without the risk of multiple pregnancy. This procedure particularly requires an objective and quantitative method to select the transferred blastocyst. Morphological evaluation using optical microscopy has, to date, been the only technique used routinely to determine the quality of mammalian embryos in practical applications and experimental work. However, such morphological evaluation is subjective and can be difficult to use for the classification of embryo quality (Scott, 2003). Therefore, more objective criteria and evaluation techniques are needed for embryos produced in vitro.

The determination of oxygen consumption activity of mammalian embryos has been studied with various techniques (Nilsson et al., 1982; Magnusson et al., 1986; Houghton et al., 1996; Overstrom et al., 1992). Recently, the oxygen consumption of a single mammalian embryo was quantified using scanning electrochemical microscopy (SECM) (Shiku et al., 2001, 2004). Using

* Corresponding author. Fax: +81 22 795 6167.
** Corresponding author at: Graduate School of Environmental Studies, Tohoku University, Aramaki Aoba 6-6-11, Sendai 980-8579, Japan.
E-mail addresses: shiku@bioinfo.che.tohoku.ac.jp (H. Shiku), matsue@bioinfo.che.tohoku.ac.jp (T. Matsue).

0956-5663/$ – see front matter © 2011 Elsevier B.V. All rights reserved.
doi:10.1016/j.bios.2011.08.037

this method, Shiku et al. found a correlation between oxygen consumption and further developmental potency indicators, such as the radius of the embryo and the ratio of blastocoel formation and hatching (Shiku et al., 2001). Likewise, Abe et al. (2008) evaluated the oxygen consumption of human embryos donated from human IVF clinics. Although these SECM techniques are fairly sensitive, unbiased, and noninvasive, the scanning system needed for the precise positioning of the microelectrode oxygen sensor is generally expensive. Furthermore, a multiple measurement procedure is needed to measure overall embryo oxygen consumption across all development stages, because the blastocyst stage embryo has inhomogeneous oxygen consumption at the inner cell mass (ICM) side and trophectoderm (TR) side (Shiku et al., 2005). More recently, Wu et al. (2007) proposed a microfluidic chip with a built-in electrode array as an alternative to probe scanning, and demonstrated the microfluidic manipulation of a single bovine embryo and the measurement of oxygen consumption based on amperometric measurement. Although microfluidic manipulation of embryos is an up-and-coming technology, as previously reported (Glasgow et al., 2001; Beebe et al., 2002; Raty et al., 2004; Zeringue et al., 2005; Park et al., 2005; Clark et al., 2005), the replacement of current techniques of embryo manipulation in clinics and laboratories, such as methods using glass capillaries with a mouthpiece, is not an urgent issue. Further, in order to perform the electrochemical measurement of oxygen consumption of embryo, the flow in the microchannel should be stopped to form a diffusion layer of oxygen near the embryo being measured.

In this study, we report the development of an integrated electrode array that enables users to determine the oxygen consumption of a single embryo, including an inhomogeneous sample such as a blastocyst, with a single measurement. Furthermore, a cylindrical micropit and cone-shaped poly(dimethylsiloxane) (PDMS) microwell on the electrode-patterned substrate are proposed to support the precise and reproducible immobilization of a glass capillary with a mouthpiece, which is routinely used for clinical, agricultural, and laboratory embryology. The oxygen consumption of single embryos at three developmental stages was determined using this electrochemical microdevice, and was compared with measurements obtained using the SECM method.

2. Experimental

2.1. Embryo collection

Female B6C3F1 mice (6–9 weeks old) were purchased from Kumagai-shigeyasu Co., Ltd. All animals were maintained in accordance with the guidelines of the Tohoku University Graduate School of Medicine, Animal Experimentation. Female mice were superovulated by giving an intraperitoneal injection of 5 IU pregnant mare serum gonadotropin (PMSG; ASKA Pharmaceutical Co., Ltd.) 92–96 h prior to two-cell stage embryo collection, followed by an intraperitoneal injection of 5 IU human chorionic gonadotropin (hCG; Yell Pharmaceutical Co., Ltd.) 44–48 h prior to collection. Females were placed with B6C3F1 males immediately after the second injection. Females exhibiting mating plugs were selected the following morning, and 44–48 h after hCG injection mice were euthanized by cervical dislocation. Oviducts were dissected and placed in human tubal fluid (HTF) medium. Two-cell stage embryos were flushed out of the oviduct with HTF medium using a 32G flushing needle. Control embryos were cultured in tissue culture dishes (Sumiron, Sumitomo Bakelite) in 50 μL droplets of KSOM medium (EmbryoMax®, Millipore Corporation) under 5 ml of light liquid paraffin (Wako Pure Chemical Industries). The dishes were prepared a day ahead of each trial and were equilibrated overnight at 37 °C in a humidified atmosphere with 5% CO_2 in air. On the day of collection, 10 two-cell embryos were washed in KSOM three times and placed in a droplet. The embryos were placed manually in the drops or microchannels using a 1.2 mm (outside diameter) borosilicate glass capillary tube (Drummond scientific company) pulled to 150–300 μm outside diameter, which was inserted into a standard mouthpiece. Cultured embryos were observed daily and the morula stage embryos were collected after 24 h of culture and blastocysts were collected after 48 h of culture.

2.2. Device fabrication

Synthetic quartz glass substrates (26 mm × 38 mm × 1.0 mm, Sendai Sekiei Ltd.) were treated with piranha solution for 30 min, and were sonicated twice in acetone for 10 min. Photoresist primer (Rohm and Haas) and positive photoresist S1818 (Rohm and Haas) were spin coated on the substrate at 3000 rpm, 30 s. The substrate was prebaked at 65 °C, 1 min; 95 °C, 5 min; and 65 °C, 3 min. The S1818 layer was exposed to UV light (365 nm) for 13 s through a photomask using a mask aligner (MA-20, Mikasa) and the substrate was developed with developer (Microposit TM MFCD-26 Developer, Rohm and Haas), and rinsed with distilled water. A Pt layer with 100–150 nm thickness was sputtered with L-332S-FH, Anelva (200 W, Ti: 5 min; Pt: 10 min) and lifted off in acetone. The substrate was further treated with oxygen plasma (Plasma Asher, Yanako, 100 W, 15 min) and N_2 gas blow. In the same manner, a SiO_2 insulator layer with 600 nm thickness was fabricated by sputtering (CFS-4ES, Shibaura, 300 W, 50 min) and lift-off photolithography in acetone overnight. The substrate was annealed in an oven at 800 °C, 60 min. The area of each of the three gate-positioned working electrodes was 10 μm × 10 μm, and the counter electrodes were 90 μm × 30 μm.

A micropit (34 μm diameter, 7 μm depth) was etched using wet etching. In short, the micropit pattern was made using photoresist S1818, as with the electrode fabrication described above. After development, a resist pattern was postbaked at 180 °C for 30 min in order to increase the resistance for glass etching, and then the bare glass surface with the micropit pattern was etched with a drop of HF buffer. The HF buffer was changed every 2 h to maintain the etching rate. The distance between the center of the micropit and each of three working electrodes is 45 μm.

The structure of a microwell consists of PDMS (SILPOT 184; Dow Corning Corp.). First, PDMS curing agent pre polymer mixture (10:1, w/w) was poured into the cell composed of cone-shaped microwells (RAP-1; Research Institute for the Functional Peptides) (Shiku et al., 2004) and cured at 80 °C for 30 min. The PDMS master was peeled off and coated with mold release agent (KF412SP; Shin-Etsu Chemical Co., Ltd.). The PDMS master was then aligned on a plastic dish, followed by pouring PDMS prepolymer up to the level at which the tip of the cone shape protrudes and cured at 80 °C for 30 min. Cured PDMS microwells were peeled off.

A PDMS stencil with 50 μm thickness and 150 μm diameter holes was fabricated using SU-8 master on a silicon wafer as previously described by Folch et al. (2000). In short, PDMS prepolymer was poured on wafer with SU-8 master. The applied PDMS was successively covered with a 130 μm-thick poly(ethylene terephthalate) (PET) sheet (PF-3R-A4; Suhayato) and clamped with an acrylic resin block to ensure firm contact with the PET film on the top surface of the SU-8 master. The PDMS and acrylic resin block were heated to 80 °C for curing for 30 min. The PDMS stencil was peeled off from the silicon wafer and cut. The electrode patterned substrate, PDMS microwell, and PDMS stencil were exposed to oxygen plasma (Plasma Asher, Yanako, 100 W, 15 s) and aligned under a microscope (TE300; Nikon) and permanently bonded.

2.3. Apparatus

All electrochemical measurements were performed with a multi-channel potentiostat (HA-1010mM8; Hokuto-Denko Corp.). Two-electrode configuration with Ag/AgCl as a reference and counter electrode was used for measurements.

2.4. Oxygen measurement using microelectrode array

The sensitive area of the integrated electrode array and the Ag/AgCl electrode were immersed in 150 ml of PBS solution and compared with a standard dissolved oxygen sensor (DO5509; Fuso-Rikaseihin) at room temperature. For detection of the oxygen reduction current, the electrode potential was held at −0.5 V vs. Ag/AgCl. The dissolved oxygen concentration was changed by adding 1 M Na_2SO_3 to PBS solution with continuous stirring. The oxygen reduction current reflecting the dissolved oxygen concentration was recorded 2 min after each addition of Na_2SO_3. The dissolved oxygen concentration was simultaneously determined with the oxygen sensor.

2.5. Oxygen consumption measurement of single mouse embryo using amperometric detection

The mouse embryos to be measured were transferred to a droplet of measurement medium (ERAM-2) on a 35-mm tissue culture dish and washed. Each embryo was observed under a microscope and its diameter was measured for further analysis. The PDMS microwell was filled with ERAM-2 and the device was placed on the stage of an optical microscope (TE300, Nikon) to observe the embryo. The potential of each working electrode was held at −0.5 V vs. Ag/AgCl for simultaneous measurement of the oxygen concentration at three different points near the surface of the embryo. After the current was stabilized, an embryo was transferred to the PDMS microwell filled with medium using a glass capillary with mouthpiece under a microscope to immobilize it at the micropit placed at the center of the integrated electrode array by means of gravity sedimentation.

2.6. Estimation of oxygen consumption based on spherical diffusion theory

The current profile recorded during the measurements reflects the change of oxygen concentration and the transient background current. Therefore, the background current profile was subtracted from the recorded current profile in order to perform an accurate estimation, according to the procedure shown in Fig. 1. Fig. 1a shows the uncorrected current during the embryo sample introduction and removal at −0.5 V. The current values before introduction (BG1) and after removal of the embryo being measured (BG2) were used for background correction. In this case, BG1 was calculated from the currents for 60 s before the introduction (t = 0–60 s in Fig. 1b), and BG2 for 60 s from 600 s after the removal (t = 1380–1440 s in Fig. 1b).

Two periods of the current profile before introduction (BG1) and after removal of the embryo being measured (BG2) were applied for the background correction. In this case, BG1 was recorded for 60 s from 60 s before introduction (t = 0–60 s in Fig. 1b), and BG2 was recorded for 60 s from 600 s after removal (t = 1380–1440 s in Fig. 1b). We assumed the background current (BG) was linearly changed during the measurement. The corrected current profile ($I(t)_{correction}$), calculated by subtraction of the profile ($BG(t)$), is expressed as

$$I(t)_{correction} = I(t) - BG(t) \quad (1)$$

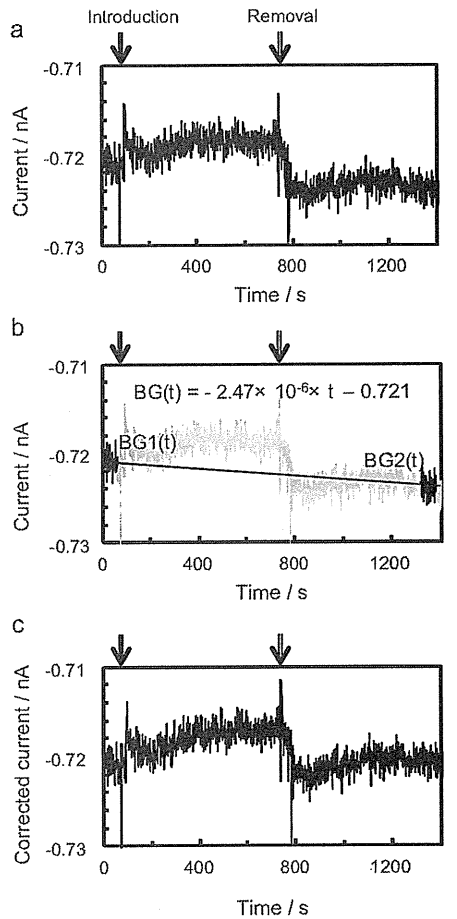

Fig. 1. (a) Uncorrected current profile recorded during measurement. A single embryo was introduced to the microdevice at 60 s and removed at 720 s. (b) Background current profile. $BG(t)$ is a linear line obtained from the all background current data ($BG1$ and $BG2$, black). (c) Corrected current profile by subtraction of the background current profile ($BG(t)$) from recorded current profile.

where $I(t)$ is uncorrected current profile, and $BG(t)$ is obtained from all the $BG1$ and $BG2$ data according to the method of least squares. This correction procedure with the two background periods is far superior to previous methods (Wu et al., 2007), which neglected background current. The difference between the currents with and without the sample (ΔI) is expressed as follows:

$$\Delta I = I^* - I_L \quad (2)$$

where I^* is the average of the corrected current recorded for 60 s before sample introduction which corresponds to the response for oxygen concentration in bulk. I_L is defined as the average of the corrected current recorded for 60 s from 600 s after the sample introduction (t = 660–720 s) in Fig. 1c. Owing to the size and shape of the sample embryo, the concentration profile around the embryo sample formed a hemispherical shape and reached a steady state within 600 s (Shiku et al., 2001, 2004; Wu et al., 2007). The oxygen concentration (C_L) with sample is expressed as follows:

$$C_L = C^* \left(\frac{I_L}{I^*}\right) \quad (3)$$

where C^* is 0.209 mM, the oxygen concentration of the air-saturated aqueous solution at room temperature. The difference

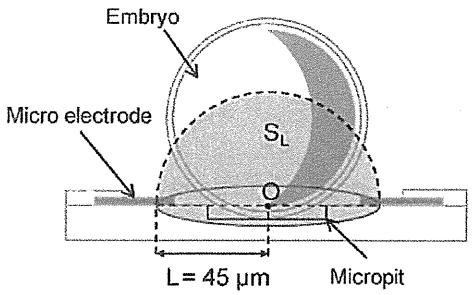

Fig. 2. A schematic view of measurement for an embryo with spherical shape immobilized on the micropit. Point O indicates the center of the microdevice. L (=45 μm), the distance from point O to the electrode; S is the area of a part cut out by flat substrate from the sphere with radius of L.

in oxygen concentration between the bulk and the area near the sample (ΔC) is expressed by

$$\Delta C = C^* - C_L = C^* \left(\frac{\Delta I}{I^*}\right) \quad (4)$$

The sample, with a spherical shape, was immobilized in the micropit at a depth of 7 μm. The spherical oxygen diffusion region (or oxygen consumption region) around the sample was formed on a horizontal substrate. The point O was defined as the center of hemispherical diffusion as in Fig. 2. The area (S_L) of a part cut out by the flat substrate from the sphere with radius of L is expressed by

$$S_L = 2\pi L^2 \quad (5)$$

where L is defined as the distance from point O to the electrode as shown in Fig. 2. In this study, L was a fixed value, 45 μm. The flux density f_L [mol s^{-1} cm^{-2}] at L and total oxygen consumption of the measured sample F [mol s^{-1}] are given by the following equations:

$$f_L = \frac{D\Delta C}{L} = \frac{D(C^* - C_L)}{L} \quad (6)$$

$$F = S_L \times f_L = 2\pi LD\Delta C = 2\pi LD(C^* - C_L) \quad (7)$$

where D is 2.10×10^{-5} cm^2 s^{-1} at room temperature, the diffusion coefficient of oxygen. It is noteworthy here that F is constant for any value of L only when the oxygen concentration profile is in accordance with an ideal hemispherical diffusion (Shiku et al., 2001, 2004; Wu et al., 2007).

2.7. SECM measurement

An SECM probe scanning technique was used to estimate single embryo oxygen consumption for comparison (Shiku et al., 2004; Aoyagi et al., 2006). The embryos measured using the micro device were transferred to a cone-shaped microwell and positioned at the lowest point. The microelectrode held at −0.5 V vs. Ag/AgCl was located at the side of the embryo sample and scanned at 160 μm, with a scan rate of 14.7 μm s^{-1}. Scanning on different sides of the embryo was performed twice at room temperature. The current reflects the local oxygen concentration near the embryo and the mass transfer rate for oxygen was estimated on the basis of Fick's law and spherical diffusion theory (Shiku et al., 2004; Aoyagi et al., 2006).

3. Results and discussion

Fig. 3 shows photographs of the electrodes patterned on the quartz substrate, and a cross section of the microwell. The magnified view of the microwell (Fig. 3a) indicates three platinum working electrodes (WE1, WE2, and WE3), a large platinum electrode (not used in this study), a circular SiO_2 insulator layer (100 μm diameter), and a cylindrical micropit (34 μm diameter, 7 μm depth). The SiO_2 insulation layer was used not only for multiple use but also for biocompatibility to minimize invasive influences. Furthermore, an SiO_2 insulating microelectrode provides low electrical noise and a stable background current compared with other materials such as polymer based insulators (Berberian et al., 2009). A mouse embryo (B6CF3F1) and the bottom of the PDMS well (150 μm diameter) are also shown in Fig. 3b and Fig. S1, Fig. S2 in Supplementary Data.

A measuring solution was introduced into the microwell where the Ag/AgCl reference electrode was inserted and electrically connected with the working and counter electrodes. A single mouse embryo was transferred into the PDMS microwell filled with measurement medium using a glass capillary with mouthpiece and immobilized at the center of the electrode array by means of gravitational sedimentation (Fig. 3c).

Fig. 4a shows a cyclic voltammogram (CV) of the three working electrodes was obtained in a 0.1 M KCl solution containing 4 mM $K_4[Fe(CN)_6]$ at a potential scan rate of 20 mV s^{-1}. The CV shows the almost steady-state limited currents in the positive potential regions, and the currents at +0.7 V vs. Ag/AgCl for WE1, WE2, and WE3 were found to be 3.51, 2.59, and 2.99 nA, respectively. Slight differences in the current of each electrode did not affect the monitoring of the local redox concentration. Generally, the radius of the electrode was estimated using the equation for a steady-state diffusion limited current at a microdisk electrode (Li et al., 2010). The estimated apparent radii of each electrode were 3.5, 2.6, and 3.0 μm, respectively, which were a little bit smaller than the electrode dimension designed.

The active areas of the electrode array and Ag/AgCl electrode were immersed in PBS solution for measurement of dissolved oxygen. Fig. 4b shows a calibration curve for dissolved oxygen in PBS solution was obtained using a one of the three Pt midroelectrodes (WE1). The dissolved oxygen concentration was determined using the conventional oxygen sensor. Dissolved oxygen was controlled by adding 1 M Na_2SO_3 solution. The oxygen reduction current before normalization was −1.22 nA. Good linearity between the normalized current and dissolved oxygen concentration was observed with a correlation coefficient (R^2) of 0.9638. Therefore, the oxygen concentration near the electrode was calculated from the current difference using Eq. (3).

The current change from 60 s before the introduction of a single mouse embryo into the center of the PDMS microwell was measured. Before the embryo sample was introduced into the microdevice, the potentials of the three working electrodes were held at −0.5 V vs. Ag/AgCl to monitor the oxygen reduction current. Generally, at least 10 min was required until the current value became stable. A single mouse embryo was introduced into the PDMS microwell and was immobilized at the center of the well by utilizing a mouse piece-assisted glass pipette under microscopic observation and gravity sedimentation. We did not use any manipulation system, such as a mechanical manipulator or microfluidics, but manually dropped an embryo sample onto the PDMS microwell.

The background current is not always stable in measurements using a band microelectrode, unlike measurements using SECM or SVET (scanning vibration electrode technique), and the variation of background current throughout the measurement sometimes reached almost 10% of the initial current. The uncorrected current profile during morula measurement is shown in Fig. 1a. Two ranges of current profiles without samples, BG1 recorded for 60 s before introduction and BG2 recorded for 60 s from 600 s after the introduction, were defined as shown in Fig. 1b. The baseline of the corrected current was almost in parallel with the t-axis as shown in Fig. 1c.

Normalized current profiles ($I(t)_{correction}/I^*$) recorded simultaneously with the integrated three-electrode array are shown in

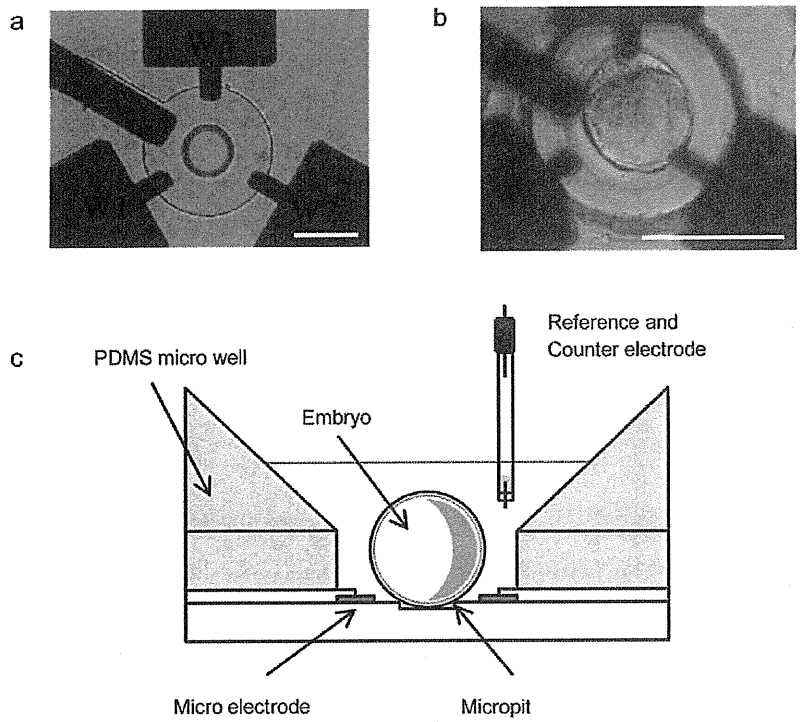

Fig. 3. (a) Layout of integrated electrode. Three platinum working electrodes (WE1, WE2, and WE3), a circular SiO_2 insulator layer, and a cylindrical micropit were patterned on quartz substrate. (b) A single mouse embryo immobilized on micropit. (c) Schematic cross section of micro device filled with measurement solution and measured embryo, together with reference and counter electrode. The scale bars in the figures correspond to 100 μm.

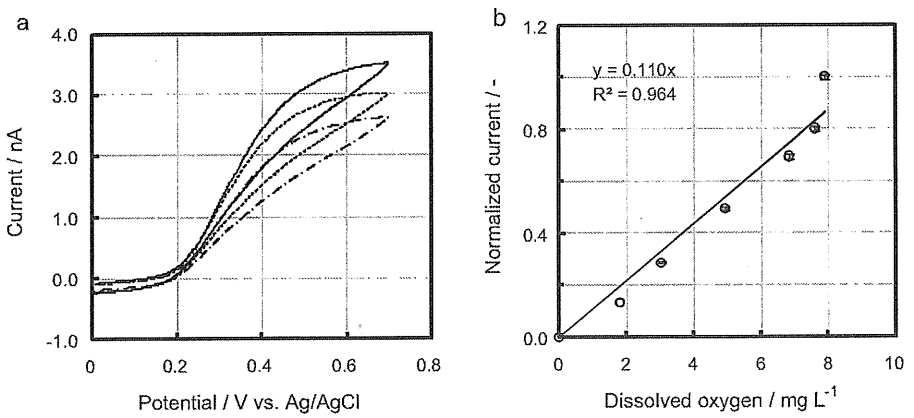

Fig. 4. (a) Cyclic voltammogram of three platinum working electrodes obtained at 20 mV s^{-1} in the solution containing 4 mM $K_4[Fe(CN)_6]$ and 0.1 M KCl as electrolyte. The solid line, dashed line, and dash-dot line were recorded from WE1 to WE3, respectively. (b) Calibration curve for dissolved oxygen in PBS solution using a one of the three Pt microelectrodes (WE1). The oxygen reduction current was recorded at a potential of −0.5 V vs Ag/AgCl.

Fig. 5a. When the morula was introduced, spike noises due to the motions of the sample and surrounding solution were initially observed. A decrease in the normalized current of less than 1.0% was recorded with a high reproducibility. Although the current generally reached a steady state within 120 s, we defined the current difference (ΔI) by measuring the currents before and 600 s after sample introduction as described in the experimental section. The oxygen concentration difference (ΔC) at the working electrode was estimated using Eq. (4). When the sample was removed, the current returned to the baseline. The flux, f_L [mol s^{-1} cm^{-2}], at S_L (see Fig. 2) and total oxygen consumption of the sample, F [mol s^{-1}], are given by Eqs. (6) and (7), respectively. The F values of the morula and fixed embryo were the same and found to be 0.75×10^{-15} mol s^{-1} in this case. This calculation procedure based on the model of spherical diffusion is quite simple because the estimation of the radius of the embryo being measured is not necessary. For each embryo sample, the ΔC and F values were obtained as the mean of the three electrodes, WE1, WE2, and WE3.

Fig. 5b shows the oxygen consumption rates of mouse embryos at three different developmental stages. The oxygen consumption rates measured with a conventional SECM-based instrument with a cone shape well are also shown. Both measurements were performed at room temperature (25 °C). The average oxygen consumption rates of two-cell, morula, and blastocyst stage embryos measured by integrated electrochemical device were $1.36 \pm 0.33 \times 10^{-15}$ mol s^{-1} ($N=5$), $1.38 \pm 0.58 \times 10^{-15}$ mol s^{-1} ($N=7$), and $3.44 \pm 2.07 \times 10^{-15}$ mol s^{-1} ($N=8$), respectively. The oxygen consumption rate at the

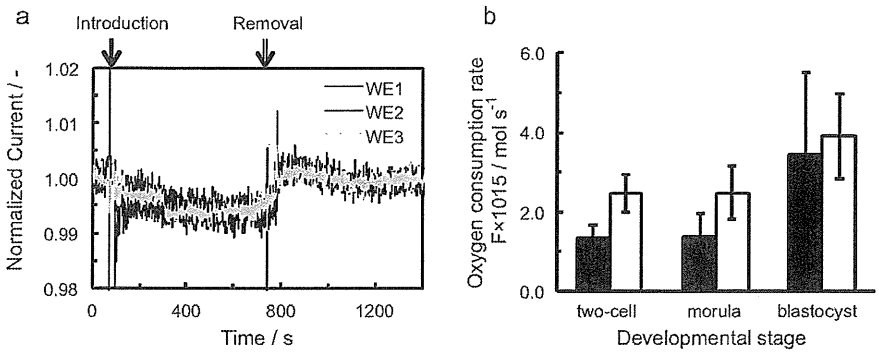

Fig. 5. (a) Normalized current profiles recorded with the integrated three-electrode array. The spike noises due to the motions of the sample and surrounding solution were observed at the introduction and removal of the measured embryo. A decrease in the normalized current of less than 1.0% was recorded 600 s after embryo introduction. (b) Oxygen consumption rates of a single mouse embryo at three developmental stages. The filled and open bars indicate the results measured by the integrated electrochemical microdevice and those measured by SECM. The error bars illustrate the standard deviations. A significant difference between the blastocyst stage and the earlier morula stage was observed using a *t*-test ($P < 0.05$).

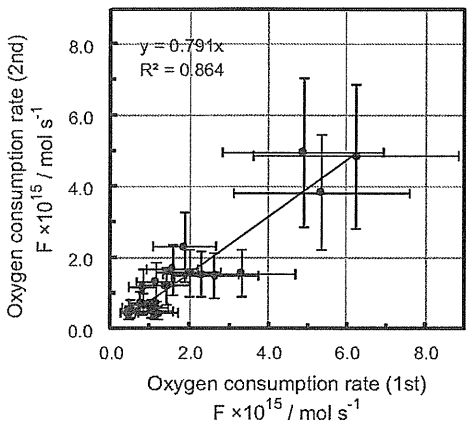

Fig. 6. Relationship between the first and second oxygen consumption measurements at an interval of almost 30 min. The line was determined by the method of least squares. The error bars illustrate the standard deviations.

blastocyst stage was significantly higher than that at the previous morula stage (*t*-test, $P < 0.05$). This increase according to developmental stage has been associated with an increase in energy demand for compaction and blastocoel formation. Although a portion of the ATP produced in blastocyst results from glycolysis, most ATP is produced by mitochondrial phosphorylation, consuming oxygen. The increasing pattern of oxygen consumption from morula to blastocyst is similar between the results of the electrode device and the conventional SECM. On the other hand, the values at each developmental stage measured with the electrode device were lower than those measured with SECM. This underestimation of oxygen consumption is explained by the deformation of the diffusion layer near the spherical sample and the extremely close position of the working electrodes to the sample.

Finally, we compared the two oxygen consumption measurements for the same embryo at an interval of almost 30 min as shown in Fig. 6. Linear regression between the two data sets yielded a correlation coefficient (R^2) of 0.864 ($N = 19$). Furthermore, the slope of the regression line was 0.791, indicating a decrease of approximately 20% in oxygen consumption rate between the first and second measurements. This result shows the degradation in the cellular activity throughout the measurement and interval of measurement at room temperature, although all the embryo samples measured with this device at room temperature resulted in further developmental progress to reach the blastocyst stage. It is well known that long periods of in vitro manipulation of mammalian embryos at room temperature causes cellular damage. Therefore, a temperature-controlled system at physiological temperature is required for practical applications of this device in the future.

4. Conclusion

An integrated electrochemical microdevice for practical oxygen consumption measurement was fabricated. The device, with an integrated electrode array, enables rapid and accurate measurement of a mouse embryo. Each single mouse embryo was immobilized at the center of an integrated electrode array in a PDMS microwell by means of a conventional glass capillary, with a mouthpiece, for handling embryos. The current responses were corrected by considering the background current during the entire measurement. The spherical diffusion model was applied to obtain accurate and simple estimation of oxygen consumption of single embryos. A significant increase in oxygen consumption reflecting the embryonic development from the morula stage to blastocyst was observed. The consumption pattern observed with the present device agreed well with that found by using the conventional SECM method. The measurement of oxygen consumption using this electrochemical device seems to be accurate, practical, and user-friendly for reproductive technicians, compared with previous oxygen consumption measurement systems. Combining the measurement of embryo oxygen consumption with other criteria, such as morphological evaluation, will provide new information regarding the subsequent viability of single embryos and improve the selection of superior embryos before embryo transfer.

Acknowledgements

This research is partly supported by the Cabinet Office, Government of Japan, through its "Funding Program for Next Generation World-Leading Researchers" (H.S.); Special Coordination Funds for Promoting Science and Technology, Formation of Innovation Center for Fusion of Advanced Technologies, from the Japan Science and Technology Agency; and also a Grant-in-Aid for Scientific Research (22245011, 21685008, and 21106502).

Appendix A. Supplementary data

Supplementary data associated with this article can be found, in the online version, at doi:10.1016/j.bios.2011.08.037.

References

Abe, H., Yokoo, M., Shiku, H., Matsue, T., Kumasako, Y., Utsunomiya, T., 2008. The 3rd International Workshop on Approaches to Single-Cell Analysis , September 11–12. ETH, Zurich, Switzerland.

Aoyagi, S., Utsumi, Y., Matsudaira, M., Yamada, H., Kacchi, M., Shiku, H., Abe, H., Hoshi, H., Matsue, T., 2006. Bunseki Kagaku 55, 847–854.

Beebe, D., Wheeler, M., Zeringue, H., Walters, E., Raty, S., 2002. Theriogenology 57, 125–135.

Berberian, K., Kisler, K., Fang, Q., Lindau, M., 2009. Anal. Chem. 81, 8734–8740.

Clark, S.G., Haubert, K., Beebe, D.J., Fergusona, C.E., Wheeler, M.B., 2005. Lab. Chip 5, 1229–1232.

Folch, A., Jo, B.H., Hurtado, O., Beebe, D.J., Toner, M., 2000. J. Biomed. Mater. Res. 52, 346–353.

Glasgow, I.K., Zeringue, H.C., Beebe, D.J., Choi, S.J., Lyman, J.T., Chan, N.G., Wheeler, M.B., 2001. IEEE Trans. Biol. Eng. 48, 570–578.

Houghton, F.D., Thompson, J.G., Kennedy, C.J., Leese, H.J., 1996. Mol. Reprod. Dev. 44, 476–485.

Li, T., Su, L., Hu, W., Dong, H., Li, Y., Mao, L., 2010. Anal. Chem. 82, 1521–1526.

Magnusson, C., Hillensjo, T., Hamberger, L., Nilsson, L., 1986. Hum. Reprod. 1, 183–184.

Nilsson, B.O., Magnusson, C., Widehn, S., Hillensjo, T., 1982. J. Embryol. Exp. Morphol. 71, 75–82.

Overstrom, E.W., Duby, R.T., Dobrinsky, J., Roche, J.F., Boland, M.P., 1992. Theriogenology 37, 269.

Park, J., Jung, S.H., Kim, Y.H., Kim, B., Lee, S.K., Park, J.O., 2005. Lab. Chip 5, 91–96.

Raty, S., Walters, E.M., Davis, J., Beebe, D.J., Rodriguez-Zas, S.L., Wheeler, M.B., 2004. Lab. Chip 4, 186–190.

Scott, L., 2003. Hum. Reprod. Update 9, 237–249.

Shiku, H., Shiraishi, S., Ohya, H., Matsue, T., Abe, H., Hoshi, H., Kobayashi, M., 2001. Anal. Chem. 173, 3751–3758.

Shiku, H., Shiraishi, S., Aoyagi, S., Utsumi, Y., Matsurida, M., Abe, H., Hoshi, H., Kasai, S., Ohya, H., Matsue, T., 2004. Anal. Chim. Acta 522, 51–58.

Shiku, H., Torisawa, Y., Takagi, A., Aoyagi, S., Abe, H., Hoshi, H., Yasukawa, T., Matsue, T., 2005. Sens. Actuators B 108, 597–602.

Wu, C.C., Saito, T., Yasukawa, T., Shiku, H., Abe, H., Hoshi, H., Matsue, T., 2007. Sens. Actuators B 125, 680–687.

Zeringue, H.C., Rutledge, J.J., Beebe, D.J., 2005. Lab. Chip 5, 86–90.

Analyst

Dynamic Article Links

Cite this: *Analyst*, 2011, **136**, 4991

www.rsc.org/analyst

PAPER

Electrochemical chip integrating scalable ring–ring electrode array to detect secreted alkaline phosphatase†

Michiaki Takeda,[a] Hitoshi Shiku,*[a] Kosuke Ino[a] and Tomokazu Matsue*[ab]

Received 19th July 2011, Accepted 9th September 2011
DOI: 10.1039/c1an15620a

An electrochemical platform for parallel monitoring of secreted alkaline phosphatase (SEAP) has been microfabricated on a device with a mammalian-cell array chip. A 4 × 4 ring–ring electrode array was designed at the rim of the round cellular pattern with a diameter of 270 μm. Electrochemical characterization was carried out, and it was found that the collection efficiency was about 50% in dual mode when the inner-ring and the outer-ring electrodes were selected as the collector and generator electrodes, respectively. The current amplification ratio for the dual mode normal to single mode was 2.84. SEAP expressing from the cells was parallelly monitored by using a multiplexer switching system at the 16 round cellular spots. The reduction current for HeLa cells transfected with plasmid encoding SEAP observed at the collector outer ring electrode was found to be significantly higher than that for wild-type HeLa. Finally, the top of the microwell with the round cellular pattern was covered with a poly(dimethylsiloxane) block for 5 min to accumulate the secreted enzyme and the product of the enzyme reaction so that further signal enhancement could be observed.

1. Introduction

Microarray technology has shown great potential and significantly impacted the field of biotechnology, from fundamental biology to clinical applications, by utilizing not only DNA chips[1–5] but also proteins,[6–10] ligand molecules,[11,12] and living cells.[13–22] Previously, we had invented a new scalable electrode array to amplify signals on the basis of redox cycling to visualize the local electrochemical nature within a minute per image that allows rapid and high-throughput electrochemical bioassays.[23,24] In a generation collection (GC) experiment (dual mode), face-to-face location with generator and collector microband electrode allows highest collection efficiency.[23–25] In addition to microband arrays, combinations of the microband and arch-shaped band electrodes,[26] and interdigitated array (IDA) electrodes[27] have been demonstrated by our group in order to improve the accessibility of samples, stimuli, and product signals and to improve the electrochemistry-based bioassay applications.

In the present study, the ring–ring electrode configuration with a relatively large dimension (>300 μm diameter) is selected to monitor responses from monolayer cells because using this configuration is one of the major detection methods in a GC experiment[28–33] to simultaneously realize the significant response amplification, ease of use, and a relatively definitive fabrication process. The round pattern of the cell monolayer was formed to express secreted alkaline phosphatase (SEAP) as a reporter protein that catalyzes the hydrolysis of *p*-aminophenylphosphate (PAPP) to *p*-aminophenol (PAP).[34] Redox cycling between PAP oxidation and *p*-quinoneimine (PQI) reduction amplifies the currents at the surrounding generator and collector electrodes (Fig. 1).[35,36] This assay can be parallelly evaluated at the 4 × 4 array consisting points of four row electrodes (ch1, ch2, ch3, and ch4) and four column

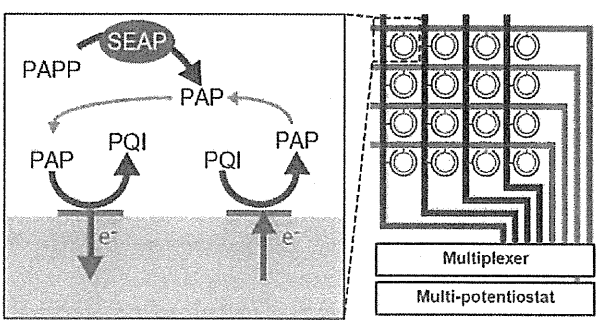

Fig. 1 Schematic illustration of the experimental system with the scalable ring–ring electrode array to detect secreted alkaline phosphatase (SEAP).

[a]*Graduate School of Environmental Studies, Tohoku University, 6-6-11, Aramaki, Aoba, Sendai, 980-8579, Japan. E-mail: shiku@bioinfo.che.tohoku.ac.jp; matsue@bioinfo.che.tohoku.ac.jp*
[b]*WPI Advanced Institute of Materials Research, Tohoku University, 2-1-1 Katahira, Aoba, Sendai, 980-8577, Japan*

† Electronic supplementary information (ESI) available: The fabrication process of the scalable ring–ring electrode array device (Fig. S1), photographs and magnified view of the device (Fig. S2), electrochemical images of the reduction current response for the scalable ring–ring electrode array device with different dimensions on a single chip device (Fig. S3) and round cellular spot before and after removing off the PDMS stencil (Fig. S4). See DOI: 10.1039/c1an15620a

electrodes (ch5, ch6, ch7, and ch8). Each channel features four inner-ring electrodes or four outer-ring electrodes and the lead electrode part. A multiplexer (switching device) and an AD/DA converter are used for electrochemical imaging on the basis of redox cycling under the control of a home-build program (Fig. 1). A highly sensitive detection of the SEAP reporter expression from adherent cells is achieved by the assembly of the following three technologies: (1) scalable electrode array to amplify signals on the basis of redox cycling, (2) cellular patterning using a stencil,[37,38] and (3) confined space of sub-nanolitre volume of the microwell to accumulate the product of enzymatic reaction.[39–44]

2. Materials and methods

2.1 Reagents

p-Aminophenylphosphate (PAPP) monosodium salt was purchased from LKT Laboratories Inc. or donated by Prof. Uichi Akiba from Akita University.[38] Ferrocenemethanol (FcMetOH; Aldrich), *p*-aminophenol (PAP; Wako Pure Chemical Industries), *N*-cyclohexyl-2-aminoethanesulfonic acid (CHES; Dojindo Laboratories, Japan), RPMI-1640 (Gibco Invitrogen, Tokyo, Japan), fetal bovine serum (FBS; Gibco), SU-8 (Microchem, CA), and other chemicals were used as received.

2.2 Device fabrication

A glass slide (50 mm × 30 mm) was treated with piranha (H_2SO_4 : 30% H_2O_2 = 3 : 1) for 15 min and washed subsequently with milli-Q water, acetone, and 2-propanol under sonication. The glass slide was then treated with O_2 plasma (LTA-101, Yanaco, 100 W, 13.6 MHz, 2 min, O_2 flow rate of 40 mL min ^{1}). Photoresist S1818 was spin coated. The first Ti/Pt layer was sputtered (Ti/Pt = 50/100 nm) to fabricate an electrode pattern after the lift-off process. An inner ring with a lead electrode and an outer ring without a lead electrode were fabricated (Fig. S1A, ESI†). A round microwell was microfabricated by wet etching. The center of the ring–ring electrode was soaked in HF for 90 min. A mixture of SU-8 3005 photoresist and SU-8 developer (1 : 1 (v/v)) was spin coated (3000 rpm, 30 s), developed, and hard-baked at 180 °C for 30 min (Fig. S1B†). The glass slide was treated with O_2 plasma, and the second Ti/Pt layer was sputtered (Ti/Pt = 50/100 nm) to fabricate the lead electrode of the outer ring. Lift-off was done using acetone (Fig. S1C†). Finally, an insulator layer of SU-8 3005 was formed and hard-baked at 180 °C for 30 min (Fig. S1D†). The total thickness of the photoresist double layer was 5.4 μm. The typical dimensions of the ring–ring electrode were as follows: inner-ring electrodes with a width of 10 μm (310 μm i.d.; 330 μm o.d.), outer-ring electrodes with a width of 15 μm (340 μm i.d.; 370 μm o.d.), and a gap of 5 μm between the ring–ring electrodes. Fig. S2† shows the design and photograph of the device. We also designed four different types of the ring–ring electrode, and the results are shown in Fig. S3†.

2.3 Cell culture

HeLa cells were transfected with commercially available plasmid vector pSEAP2-control (Clontech Laboratories Inc., CA).[38–41,45] Cells were seeded in a 35 mm dish at a density of 5 × 10^5 cells mL ^{1} of RPMI-1640 containing 10% FBS. A day after the culture, transfection was performed by adding 500 μL of Opti-MEM 1 medium (Gibco) containing 4 μg of plasmid DNA and 10 μL of Lipofectamine 2000 (Invitrogen). Incubation was carried out for 5 h. Subsequently, the transfection medium was changed to a pure culture medium, and the cells were incubated at 37 °C overnight. The transfected HeLa cells (HeLa-SEAP) were patterned on the electrode array device in the 4 × 4 array of circles with a diameter of 300 μm by using a poly(dimethylsiloxane) (PDMS) stencil. The preparation process for the PDMS stencil sheet is given elsewhere.[37,38] Holes were made using SU-8 mold. Importantly, the PDMS stencil covered the surface of the ring–ring electrodes until electrochemical characterization was performed. HeLa-SEAP was seeded on the PDMS stencil-attached device with 2.6 × 10^6 cells mL ^{1} and cultured at 37 °C in RPMI-1640 containing 10% FBS for 6 h (Fig. S4†). The PDMS stencil was removed to expose the electrode detector to the solution. Owing to the size of the cylindrical well microfabricated by wet-etching, *i.e.*, a depth of 11 μm and a diameter of 267 μm, cell monolayer patterns were clearly formed after the removal of the PDMS stencil. CHES buffer (20 mM CHES, 135 mM NaCl, 4.0 mM KCl, 5.6 mM glucose, 0.49 mM $MgCl_2$ (pH 9.5)) containing 4.7 mM PAPP was used for electrochemical measurement of cellular arrays. The electrodes were stabilized for 10 min after the PDMS stencil was removed.

2.4 Electrochemical measurement

A multi-potentiostat (HA-1010mM4, Hokuto Denko Corp., Tokyo, Japan) was used to perform potential step chronoamperometry. Potential control and current acquisition were performed using a personal computer *via* an AD/DA board (PXI-6723, National Instrument, Austin, TX) and a multiplexer (PXI-2529, National Instrument, Austin, TX). An Ag/AgCl electrode and Pt electrodes were used as the reference electrode and counter electrodes, respectively. Electrochemical imaging was performed at a pixel resolution of 4 × 4 pixels by using a program developed by LabView soft ware.[27] Initially, the potential of all the eight channels was set at 0.0 V, and the base line current was recorded. The potential of the first row electrode was stepped to +0.3 V for 6.0 s. The current values for the four column electrodes were sequentially recorded with a read-out time of 20 ms (80 ms in total). Next, the potential of the second row electrode was set at +0.3 V, whereas that of the first row electrode was stepped back to 0.0 V. In the same manner, the potential of the third and the fourth row electrodes was sequentially set at +0.3 V. It takes 24.32 s to obtain the electrochemical data of 16 points.

3. Results and discussion

This study introduces a highly sensitive electrochemical device chip based on redox cycling, which facilitates rapid and high throughput assays. This device features four row electrodes (ch1, ch2, ch3, and ch4) and four column electrodes (ch5, ch6, ch7, and ch8). The inner and outer rings were connected to the row and column electrodes, respectively. Redox cycling only occurs between the ring–ring electrodes; the other area was covered with

photoresist SU-8. Responses enhanced by redox cycling were recorded sequentially using a multiplexer. Cell culture and SEAP monitoring were carried out in 16 microwells on the chip. The round cellular spots in the microwells were surrounded by ring–ring electrodes. The depth and the diameter of the microwell fabricated by wet etching were 11 and 267 μm, respectively (Fig. S2†). The volume of the microwell was 1.29×10^{-10} L. The inner-ring row electrodes were connected Ti/Pt line *via* overlayered on photoresist SU-8 3005.

Next, we show the basic electrochemical properties to characterize the scalable multi-electrode array. Fig. 2 shows cyclic voltammograms of the ring–ring electrode in 4.0 mM $K_4Fe(CN)_6$ and 0.1 M KCl. The potentials of all the eight channels were simultaneously scanned from 0 to 0.6 V at 20 mV s^{-1}. Each channel contained four inner-ring or four outer-ring electrodes. The oxidation current values at 0.6 V for the inner-ring row electrodes (ch1–4) and outer-ring column electrodes (ch5–8) were found to be 0.994 ± 0.015 ($n = 4$) and 1.23 ± 0.022 μA ($n = 4$), respectively (mean ± standard deviation). The coefficient of variation was found to be less than 2% for both row and column electrodes owing to simple and reliable lithographic procedures in chip fabrication.

Single mode experiment has been performed by potential stepping, in which the potential of the electrode was stepped from 0.0 to 0.4 V to oxidize 0.5 mM FcMetOH. As shown in Fig. 3A, the potentials of one inner-ring row electrode (one of ch1 to ch4) and four outer-ring column electrodes (all of ch5 to ch8) were all set at 0.4 V. Fig. 3B shows the response at the row electrode (working 1). Four independent experiments were performed for ch1, ch2, ch3, and ch4, and overwritten. The current response of the inner ring electrode did not reach a steady state due to a relatively large dimension (>300 μm in diameter). This behavior was similar to that of the microband electrode rather than the microring electrode.[46] The oxidation current for ch1 to ch4 was 56.73 ± 1.11 nA ($n = 4$) at $t = 15$ s (10 s after the potential step). The current for the column electrode was expressed as the summation of current in the four channels (ch5, ch6, ch7, and ch8 were all connected to working 2 of the multi-potentiostat) as shown in Fig. 3C. When ch1 was selected as a row electrode for potential stepping (working 1), the other row electrodes (ch2, ch3, and ch4) were disconnected. The disconnected electrode induces redox cycling at the crossing points with the column electrodes, resulting in complicated current behavior at the column electrode (working 2, Fig. 3C). In the same manner, redox cycling should occur at the crossing point between the other three row electrodes and the four column electrodes.

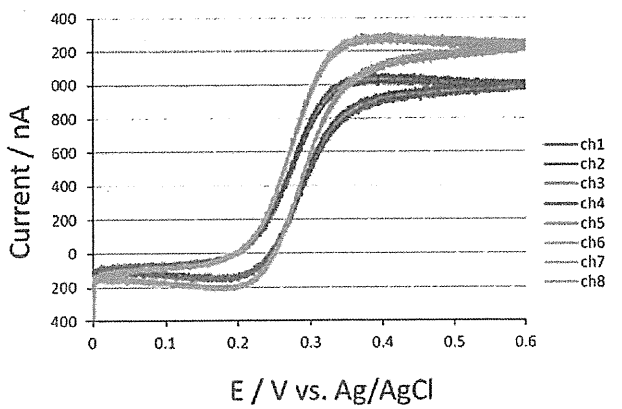

Fig. 2 Cyclic voltammograms of the inner-ring (ch1 to 4) and outer-ring electrodes (ch5 to 8) in 4.0 mM $K_4Fe(CN)_6$ and 0.1 M KCl. Scan rate: 20 mV s^{-1}.

Next, dual mode was performed by using the inner-ring row electrodes (ch1, ch2, ch3, and ch4) as the generator (Fig. 3D). The potential was stepped from 0.0 to 0.4 V for ch1, ch2, ch3, and ch4 independently. The column electrodes (outer-ring electrodes, ch5, ch6, ch7, and ch8) were all connected and used as collector electrodes, maintaining the electrode potential at 0.0 V. Fig. 3E and F show the current responses for the row (working 1) and column electrodes (working 2), respectively. As shown in Fig. 3E, the oxidation current in the row electrode increased considerably. At $t = 15$ s, the oxidation current was 161 ± 2.11 nA ($n = 4$). The collected reduction current was 79.5 ± 4.59 nA ($n = 4$). The collection efficiency was estimated to be 49.2 ± 2.36% ($n = 4$). In the column electrode (Fig. 3B and E), the current amplification ratio for the dual mode normal to single mode was 2.84. In the dual mode, the unconnected row electrodes did not induce redox cycling because the potential of the crossing column electrode was maintained at 0.0 V. Therefore, collection efficiency is a good parameter to characterize the size, design, and location of the ring–ring electrode.

The two experiments mentioned above are single and dual mode experiments focusing on inner-ring row electrodes (ch1 to ch4). We also performed GC experiments by using the outer-ring column electrode (ch5, ch6, ch7, and ch8) as the generator. The potential was stepped from 0.0 to 0.4 V for ch4, ch5, ch6, and ch7 independently (working 1). In this case, all the row electrodes (inner-ring electrodes, ch0, ch1, ch2, and ch3) were connected and used as collectors, maintaining the potential at 0.0 V (working 2). At $t = 15$ s, the oxidation current for the column electrode was 207 ± 7.19 nA ($n = 4$). The collected reduction current was 92.4 ± 5.30 nA ($n = 4$). The collection efficiency was estimated to be 44.7 ± 1.21% ($n = 4$), therefore, our results were reasonable because the collection efficiency should be high when a large collector electrode is used. The geometry of the ring–ring electrode was further optimized by comparing different geometries, including the widths of the inner-ring and outer-ring electrodes and the gap between the two electrodes. The design and the results for the device integrating four different ring–ring electrode arrays are given in the ESI†.

Next, we obtained electrochemical responses from living cells cultured in the device. HeLa cells transfected with SEAP (HeLa-SEAP) were used as a model system to monitor gene expression. Fig. 4A shows schematic view of the electrochemical response obtained at a ring–ring electrode. The transfected HeLa cells were seeded in the monolayer on the bottom of the cell culture chamber by using the PDMS stencil method. SEAP functions as a catalyst in converting the enzymatic substrate PAPP to PAP. The potential of the inner-ring row electrode was stepped to +0.3 V to oxidize PAP to PQI, and then the reduction current for PQI was recorded at the outer-ring column electrode at 0.0 V. The PQI was reduced back to re-generate PAP. Fig. 4B and C show the electrochemical images for HeLa-SEAP and

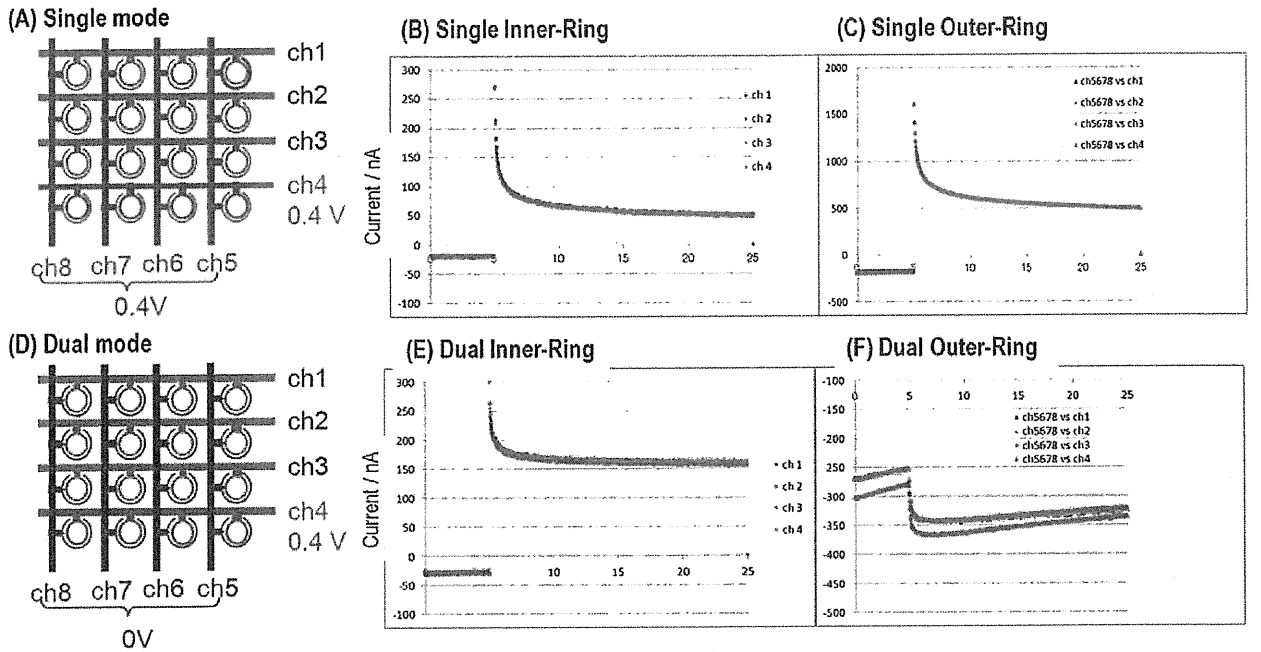

Fig. 3 (A–C) Schematic illustration (A) and current responses at inner-ring (B) and outer-ring electrodes (C) in single mode, 0.5 mM ferrocenemethanol, and 0.1 M KCl. (D–F) Schematic illustration (D) and current responses at inner-ring (E) and outer-ring electrodes (F) in dual mode, 0.5 mM ferrocenemethanol, and 0.1 M KCl.

wild-type HeLa, respectively. The images are constructed from the data array of reduction current of the collector at 6 s after the potential step at the generator. The reduction current responses of HeLa-SEAP (3.64 ± 1.84 nA (n = 16)) were significantly larger than that of wild-type HeLa (1.34 ± 0.87 nA (n = 16)) (p < 0.001 for t-test) although the reduction current

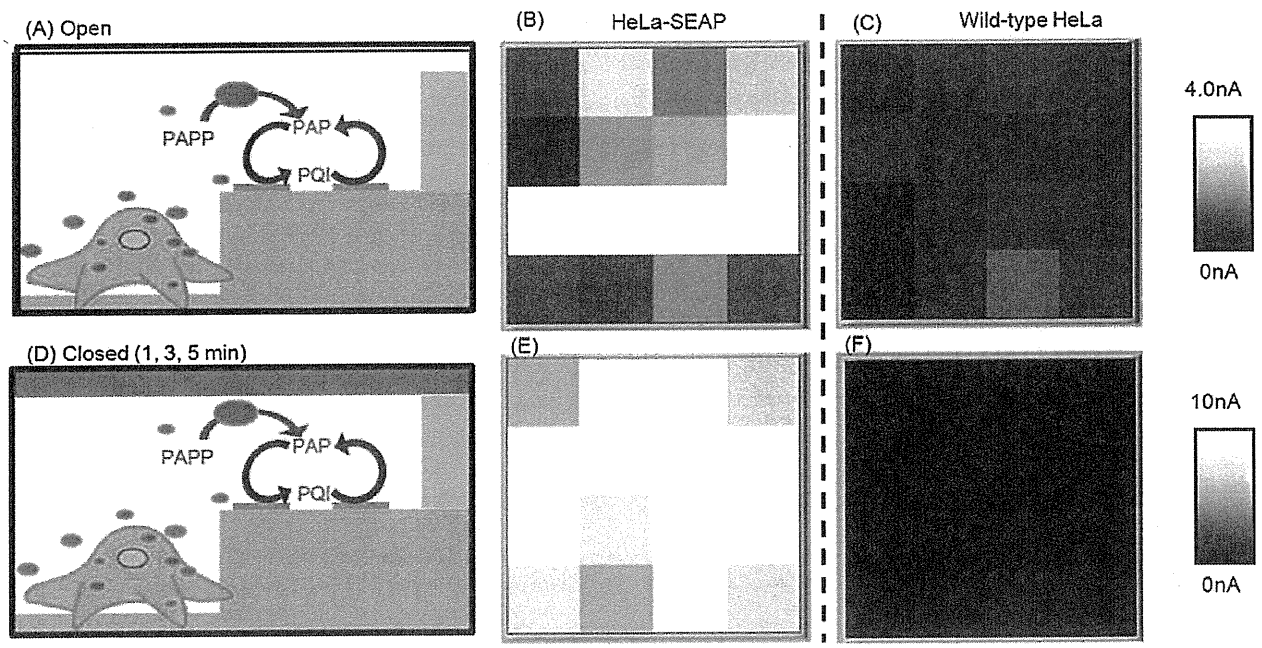

Fig. 4 (A–C) Schematic illustration to monitor SEAP expression (A), electrochemical images (16 pixels) of the reduction current response for HeLa-SEAP (B) and wild-type HeLa (C). The top of the electrode array device is "opened." (D–F) The top of the electrode array device is "closed" with a PDMS block (D). Electrochemical images of the reduction current response for HeLa-SEAP (E) and wild-type HeLa (F). Measuring solution: 4.7 mM PAPP in CHES buffer.

responses for HeLa-SEAP showed fluctuations. The responses of wild-type HeLa were not zero because of the endogenous alkaline phosphatase activity. The signal-to-noise (*S/N*) ratio was 2.71, which is defined as [response for HeLa-SEAP]/ [response for wild-type HeLa]. This *S/N* value was slightly higher than the *S/N* value previously obtained (*ca.* 2.1) by scanning electrochemical microscopy (SECM).[38] Importantly, the ring–ring based scalable electrode array can be scanned within 25 s to obtain 16 points of data whereas the SECM single-line scan takes 30 s to obtain the response for one cellular sample with a diameter of 300 μm.[38]

Finally, the top of the microwell with the round cellular pattern was covered with a PDMS block. The device was covered with the PDMS block in order to effectively detect PAP, the product of the enzymatic reaction. The reaction pathway did not change from Fig. 4A but the currents observed at the ring–ring electrodes were expected to be enhanced because both the SEAP and PAP produced in the microwell did not diffuse out (Fig. 4D). In the case where the PDMS block completely covers the PDMS microwell, electrochemical measurement is not possible because the current does not flow. However, we have noticed that there was an electric connection because of leakage of the ionic flow between the working and the reference electrodes even when almost 100% of the reactant within the microwell was consumed.[39,40] Fig. 4E and F show the electrochemical images for HeLa-SEAP and wild-type HeLa 5 min after the PDMS block was placed on the electrode array device. Fig. 5 shows the summary of the reduction current responses without (open) and with the PDMS block (closed). Response for the closed mode was 2.6-fold to 3.2-fold higher than that for open mode. The reduction current response increased with the accumulation time. The *S/N* ratio reached 12.4 for an accumulation time of 5 min. This value was the highest among the different detection schemes that we have tried thus far. However, it is noteworthy here that PAP (and also PQI) is easily degraded in the presence of oxygen. The half-life of PAP in air-saturated alkaline aqueous media was approximately 10 min.[47] Therefore, increasing the accumulation time beyond this value might not be appropriate.[40]

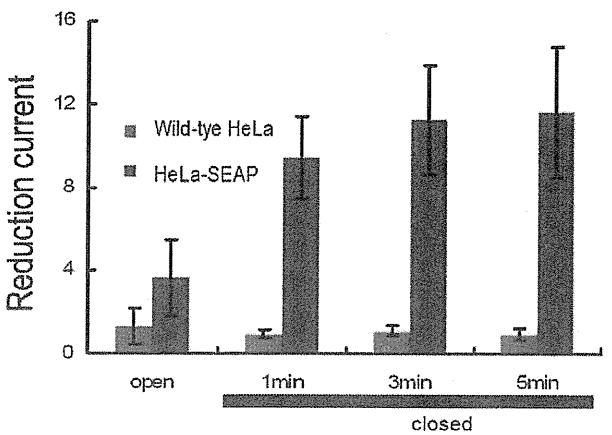

Fig. 5 Summary of cellular response.

4. Conclusions

In conclusion, a ring–ring electrode array was designed at the rim of the round cellular pattern. Electrochemical characterization of the scalable row and column electrode array was performed to indicate that this device allows effective signal amplification on the basis of redox cycling and facilitates the development of biological applications with rapid, parallel, and high reliability. The SEAP signal was detected to construct an electrochemical image within 25 s. When the microwell was covered using the PDMS block, the *S/N* ratio improved because of the accumulation of SEAP and PAP within the small volume of the microwell.

Acknowledgements

This research is partly supported by the Cabinet Office, Government of Japan through its "Funding Program for Next Generation World-Leading Researchers" (H. S.); Special Coordination Funds for Promoting Science and Technology, Formation of Innovation Center for Fusion of Advanced Technologies, from Japan Science and Technology Agency; and also a Grant-in-Aid for Scientific Research (22245011, 21685008, and 21106502).

References

1 S. P. A. Fodor, J. L. Read, M. C. Pirrung, L. Stryer, A. T. Lu and D. Solas, *Science*, 1991, **251**, 767–773.
2 M. Schena, D. Shalon, R. W. Davis and P. O. Brown, *Science*, 1995, **270**, 467–470.
3 H. Nagai, Y. Murakami, Y. Morita, K. Yokoyama and E. Tamiya, *Anal. Chem.*, 2001, **73**, 1043–1047.
4 J. M. Tam and D. R. Walt, *Biosens. Bioelectron.*, 2009, **24**, 2488–2493.
5 M. Gebala, G. Hartwich and W. Schuhmann, *Faraday Discuss.*, 2011, **149**, 11–22.
6 K. Tomizaki, K. Usui and H. Mihara, *FEBS J.*, 2010, **277**, 1996–2005.
7 D. Juncker, H. Schmid and E. Delamarche, *Nat. Mater.*, 2005, **4**, 622–628.
8 S. Higeki, K. Sada, I. Yoshimura, S. Shinkai, N. Kato and I. Hamachi, *Nat. Mater.*, 2004, **3**, 58–64.
9 G. MacBeath and S. L. Schreiber, *Science*, 2000, **289**, 1760–1763.
10 H. Shiku, T. Matsue and I. Uchida, *Anal. Chem.*, 1996, **68**, 1276–1278.
11 N. Kanoh, M. Kyo, K. Inamori, A. Ando, A. Asami, A. Nakao and H. Osada, *Anal. Chem.*, 2006, **78**, 2226–2230.
12 M. Uttamchandani, D. P. Walsh, S. Q. Yao and Y. T. Chang, *Curr. Opin. Chem. Biol.*, 2005, **9**, 4–13.
13 J. Ziauddin and D. M. Sabatini, *Nature*, 2001, **411**, 107–110.
14 K. R. King, S. Wang, D. Irima, A. Jayaraman, M. Toner and M. L. Yarmush, *Lab Chip*, 2007, **7**, 77–85.
15 K. Nagamine, S. Onodera, Y. Torisawa, T. Yasukawa, H. Shiku and T. Matsue, *Anal. Chem.*, 2005, **77**, 4278–7281.
16 Y. S. Torisawa, T. Kaya, T. Takii, D. Oyamatsu, M. Nishizawa and T. Matsue, *Anal. Chem.*, 2003, **73**, 2154–2158.
17 S. Yamamura, H. Kishi, Y. Tokimitsu, S. Kondo, R. Honda, S. R. Rao, M. Omori, E. Tamiya and A. Muraguchi, *Anal. Chem.*, 2005, **77**, 8050–8056.
18 S. Yatsushiro, S. Yamamura, Y. Yamaguchi, Y. Shinohara, E. Tamiya, T. Horii, Y. Baba and M. Kataoka, *PLoS One*, 2010, **5**, e13179.
19 J. H. Sung and M. L. Shuler, *Bioprocess Biosyst. Eng.*, 2010, **33**, 5–19.
20 M. Hosokawa, A. Arakaki, M. Takahashi, T. Mori, H. Takeyama and T. Matsunaga, *Anal. Chem.*, 2009, **81**, 5308–5313.
21 K. Ino, M. Okochi, N. Konishi, M. Nakatochi, R. Imai, M. Shikida, A. Ito and A. Honda, *Lab Chip*, 2008, **8**, 134–142.
22 R. Popovtzer, T. Neufeld, A. Popovtzer, I. Rivkin, R. Margalit, D. Engel, A. Nudelman, A. Rephaeli, J. Rishpon and Y. Shacham-Diamand, *Nanomedicine: Nanotechnology, Biology and Medicine*, 2008, **4**, 121–126.

23 Z. Lin, Y. Takahashi, Y. Kitagawa, T. Umemura, H. Shiku and T. Matsue, *Anal. Chem.*, 2008, **80**, 6830–6833.
24 Z. Y. Lin, Y. Takahashi, T. Murata, M. Takeda, K. Ino, H. Shiku and T. Matsue, *Angew. Chem., Int. Ed.*, 2009, **48**, 2044–2046.
25 Z. Y. Lin, K. Ino, H. Shiku and T. Matsue, *Chem. Commun.*, 2010, **46**, 559–561.
26 R. Kunikata, Y. Takahashi, M. Koide, T. Itayama, T. Yasukawa, H. Shiku and T. Matsue, *Sens. Actuators, B*, 2009, **141**, 256–262.
27 K. Ino, W. Saito, M. Kokide, T. Umemura, H. Shiku and T. Matsue, *Lab Chip*, 2011, **11**, 385–388.
28 E. Katelhon, B. Hofmann, S. G. Lemay, M. A. G. Zevenbergen, A. Offenhausser and B. Wolfrum, *Anal. Chem.*, 2010, **82**, 8502–8509.
29 R. Cornut, M. Mayoral, D. Fabre and J. Mauzeroll, *J. Electrochem. Soc.*, 2010, **157**, F77–F82.
30 Z. Liu, O. Niwa, R. Kurita and T. Horiguch, *Anal. Chem.*, 2000, **72**, 1315–1321.
31 S. L. R. Harvey, K. H. Parker and D. O'Hare, *J. Electroanal. Chem.*, 2007, **610**, 122–130.
32 P. Liljeroth, C. Johans, C. J. Slevin, B. M. Quinn and K. Kontturi, *Anal. Chem.*, 2002, **74**, 1972–1978.
33 O. Laczka, F. J. del Campo, F. X. Munoz-Pascal and E. Baldrich, *Anal. Chem.*, 2011, **83**, 4037–4044.
34 Y. S. Torisawa, N. Ohara, K. Nagamine, S. Kasai, T. Yasukawa, H. Shiku and T. Matsue, *Anal. Chem.*, 2006, **78**, 7625–7631.
35 Y. Jang, S. Y. Oh and J. K. Pary, *Enzyme Microb. Technol.*, 2006, **39**, 1122–1127.
36 P. J. Lamas-Ardisana, P. Queipo, P. Fanjul-Bolado and A. Costa-Garcia, *Anal. Chim. Acta*, 2008, **615**, 30–38.
37 Y. Takahashi, T. Miyamoto, H. Shiku, R. Asano, T. Yasukawa, I. Kumagai and T. Matsue, *Anal. Chem.*, 2009, **81**, 2785–2790.
38 H. Shiku, M. Takeda, T. Murata, U. Akiba, F. Hamada and T. Matsue, *Anal. Chim. Acta*, 2009, **640**, 87–92.
39 H. Shiku, S. Goto, S. Jung, K. Nagamine, M. Koide, T. Itayama, T. Yasukawa and T. Matsue, *Analyst*, 2009, **134**, 182–187.
40 H. Shiku, J. Suzuki, T. Murata, K. Ino and T. Matsue, *Electrochim. Acta*, 2010, **55**, 8263–8267.
41 H. Shiku, D. Okazaki, J. Suzuki, Y. Takahashi, T. Murata, H. Akita, H. Harashima, K. Ino and T. Matsue, *FEBS Lett.*, 2010, **584**, 4000–4008.
42 M. Koide, T. Yasukawa, K. Nagamine, H. Shiku, T. Itayama and T. Matsue, *Sens. Actuators, B*, 2011, **153**, 474–478.
43 T. W. Molter, S. C. McQuaide, M. T. Suchorolski, T. J. Strovas, L. W. Burgess, D. R. Meldrum and M. E. Lidstrom, *Sens. Actuators, B*, 2009, **135**, 678–686.
44 M. E. Vincent, W. Lin, E. B. Haney and R. F. Ismagilov, *Chem. Soc. Rev.*, 2010, **39**, 974–984.
45 Y. Takahashi, H. Shiku, T. Murata, T. Yasukawa and T. Matsue, *Anal. Chem.*, 2009, **81**, 9647–9681.
46 T. Saito, C.-C. Wu, H. Shiku, T. Yasukawa, M. Yokoo, T. Ito-Sasaki, H. Abe, H. Hoshi and T. Matsue, *Analyst*, 2006, **131**, 1006–1101.
47 E. P. Gil, H. T. Tang, H. B. Halsall, W. R. Heineman and A. S. Misleg, *Clin. Chem.*, 1990, **36**, 662–665.

View Online / Journal Homepage / Table of Contents for this issue
Dynamic Article Links

PCCP

Cite this: *Phys. Chem. Chem. Phys.*, 2011, **13**, 16569–16573

www.rsc.org/pccp

PAPER

Electrochemical detection of receptor-mediated endocytosis by scanning electrochemical microscopy

Yasufumi Takahashi,*[a] Takeshi Miyamoto,[a] Hitoshi Shiku,*[a] Kosuke Ino,[a] Tomoyuki Yasukawa,[b] Ryutaro Asano,[c] Izumi Kumagai[c] and Tomokazu Matsue*[ad]

Received 10th June 2011, Accepted 5th July 2011
DOI: 10.1039/c1cp21886g

We report a scanning electrochemical microscopy (SECM)-based receptor-mediated endocytosis detection method. Epidermal growth factor receptor (EGFR), which is one of the key membrane proteins associated with cancer, was used as a model for receptor-mediated endocytosis. EGFR molecules on the outer cell membrane were detected by SECM by using alkaline phosphatase (ALP) as a labeling enzyme. Since SECM detected the ALP activity on the outer membrane, the procedure helped discriminate the EGFR on the outer membrane from the intracellular EGFR involved in endocytosis. SECM showed a marked decrease in the current responses generated due to ALP activity by 93% on addition of the epidermal growth factor, indicating clearly that EGF triggered the endocytosis, which led to the withdrawal of most EGFRs from the outer membrane.

Introduction

Endocytosis is a process characterized by internalization of extracellular molecules followed by engulfment of these molecules by the cellular membrane to form an endocytic vesicle. Receptor-mediated endocytosis is an important process that negatively regulates the receptor-mediated signals by reducing the surface concentration of the receptor itself (down-regulation) and controls the strength and duration of the signals downstream.[1] Then, the receptor is recycled back to the plasma membrane. Epidermal growth factor receptor (EGFR) is one of the key membrane proteins associated with cancer.[2] Epidermal growth factor (EGF) binds to the EGFR, and the activated EGFR initiates the signaling cascades, thereby promoting cell proliferation, differentiation, apoptosis, and migration. This signaling is controlled by EGF-triggered endocytosis, which reduces the number of EGFR molecules exposed to the outside medium. Therefore, various methods have been established to study endocytosis of EGFR. Fluorescence measurement is an effective method for imaging of the membrane protein, but visualization of the membrane protein motion at the interface of the cellular membrane remains difficult because long-term monitoring of fluorescence signals induces photobleaching.[3] Sokolov and coworkers developed a labeling method for membrane proteins by using anti-EGFR gold nanoparticles for monitoring endocytosis. The absorption wavelengths of the nanoparticles trapped in the vesicle changed according to the interparticle center–center distance; therefore, this method was effective for monitoring the endocytosis process.[4] However, identification of the starting point of vesicle formation is quite difficult. Therefore, development of an analytical tool that allows discrimination of the EGFR molecules on the outer membrane from those of the inner endocytic vesicles is necessary. Korchev and coworkers developed scanning ion conductance microscopy (SICM) for visualizing the surfaces of living cells,[5] and SICM has been reported to be effective for visualizing the endocytic pit.[6]

Scanning electrochemical microscopy (SECM) is a useful tool for analyzing biological samples in a noninvasive manner. Since a localized chemical reaction and chemical concentration near the sample under physiological conditions can be quantitatively and noninvasively characterized as a Faradaic current by scanning the microelectrode, SECM has been applied for quantitative investigation of living cells.[7–9] The application of SECM for investigation of living cells has several advantages. First, SECM can selectively detect the cell membrane protein at the outer membrane surface.[10] In this study, the membrane protein was labeled with an enzyme-labeled antibody. Recently, this method was applied to determine the expression level of membrane glycans.[11] Simultaneous imaging of the inner and outer sides of the cell was performed by fluorescence measurement using an optical fiber electrode.[12] Second, SECM has a high temporal and spatial resolution for monitoring cellular phenomena that occur at various interfaces. Mirkin and coworkers developed a nanoelectrode and inserted the electrode into a cell for estimating the intracellular redox activity.[13]

[a] *Graduate School of Environmental Studies, Tohoku University, Aramaki, Aoba 6-6-11-605, Sendai 980-8579, Japan. E-mail: yasufumi1981@hotmail.com*
[b] *Graduate School of Material Science, University of Hyogo, 3-2-1 Kouto, Kamigori-cho, Ako-gun, Hyogo 678-1297, Japan*
[c] *Graduate School of Engineering, Tohoku University, Aramaki, Aoba 6-6-11-607, Sendai 980-8579, Japan*
[d] *Advanced Institute of Materials Research, Tohoku University, Katahira, Aoba 2-1-1, Sendai 980-8577, Japan*

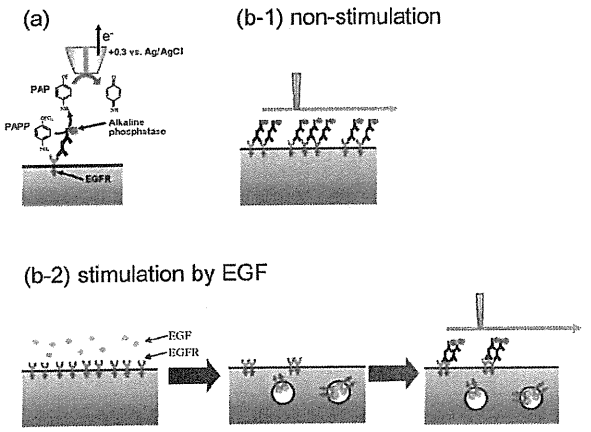

Fig. 1 (a) Schematic illustration of EGFR detection using SECM. The EGF stimulation induced endocytosis was estimated by comparing the PAP oxidation current responses of the non-stimulation (b-1) and stimulation by EGF (b-2) cells.

Wightman and coworkers performed real-time monitoring of neurotransmitter release associated with exocytosis.[14] Unwin and coworkers probed the dynamics of partitioning of electroactive solutes between two immiscible phases using SECM.[15] We estimated the degree of cell membrane permeability of the electrochemical mediator by using a microelectrode.[16] Previous studies have shown that SECM is a suitable analytical tool for monitoring various phenomena that occur at the cellular interface. However, SECM monitoring of the membrane protein motion at the cellular interface has not been reported. In this study, we used SECM to investigate EGF-triggered endocytosis (Fig. 1). EGFR was labeled with an alkaline phosphatase (ALP)-labeled antibody for electrochemical detection. The decrease in the expression level of EGFR induced by the EGF-triggered endocytosis was estimated by comparing the Faradaic current responses of the cells with and without EGF stimulation. To the best of our knowledge, this is the first study to report the detection of endocytosis by using SECM.

Experimental

Materials

Primary antibodies (mouse anti-EGFR IgG [SC-120, Santa Cruz Biotechnology, Santa Cruz, CA]), mouse anti-EGFR IgG labeled with fluorescein isothiocyanate (FITC [sc-120 FITC, Santa Cruz Biotechnology, Santa Cruz, CA]), secondary antibodies (goat anti-mouse IgG labeled with ALP [62-6522, Zymed]), Alexa Fluor® 488 EGF complex (E13345) molecular probe, recombinant human epidermal growth factor (BD Biosciences), *p*-aminophenyl phosphate monosodium salt (PAPP; LKT Lab Inc.), and poly(dimethylsiloxane) (PDMS; Dow Corning Toray Co., Ltd.) were purchased and used as received. All other chemicals were also used as received. All the solutions were prepared using distilled water obtained using a Milli-Q water system (Millipore, Japan).

Cell culture

A normal Chinese hamster ovary (CHO) and cells derived from human epidermoid carcinoma cell line A431 were donated by the Cell Resource Center for Biomedical Research (Tohoku University). The EGFR/CHO (CHO transfected with EGFR) cells used in this study were prepared according to the literature.[17] Normal CHO and A431 cells were cultured in RPMI-1640 medium (Gibco/Invitrogen, Tokyo, Japan) containing 10% fetal bovine serum (FBS; Gibco), 50 μg mL^{-1} penicillin (Gibco), and 50 μg mL^{-1} streptomycin (Gibco) at 37 °C in a humidified atmosphere containing 5% CO_2. The EGFR/CHO cells were cultured in RPMI-1640 medium (Sigma) containing 10% FBS (Gibco), and 50 μg mL^{-1} G418 (Nacalai Tesque) at 37 °C in a humidified atmosphere containing 5% CO_2.

EGFR labeling for fluorescence measurements

EGFR was visualized with a fluorescent-labeled EGF (Alexa Fluor® 488 EGF complex) or a fluorescent-labeled antibody (anti-EGFR IgG labeled with FITC). For fluorescence labeling, the cells were reacted with RPMI-1640 containing fluorescent-labeled EGF (1 μg mL^{-1}) or a FITC-labeled antibody (1 μg mL^{-1}) for 60 min at 4 °C, followed by thorough washing with RPMI-1640.

EGFR labeling with ALP for electrochemical measurements

EGFR was labeled with an ALP-labeled antibody for electrochemical detection. In the case of EGFR labeling with an ALP-labeled antibody, the cells were reacted with RPMI-1640 containing an anti-EGFR antibody (1 μg mL^{-1}) for 90 min at 37 °C, followed by thorough washing with RPMI-1640. The cells were then reacted with RPMI-1640 containing an ALP-labeled secondary antibody (ALP-labeled IgG) (1 μg mL^{-1}) for 90 min at 37 °C, followed by thorough washing with RPMI-1640.

Preparation of a cell-patterned substrate

Cell patterns were developed using the polydimethylsiloxane (PDMS) microstencil method. Linear (width, 300 μm) and circular (diameter, 500 μm) patterns of the microstencils were prepared using a CO_2 laser beam (Universal Laser Systems, Scottsdale, Arizona, USA). The cells (10^6 cells per mL, 100 μL) were seeded on a 35 mm Petri dish (Falcon), sealed with the PDMS microstencil, and incubated for 2 h to allow the cells to adhere to the dish. The excess nonadherent cells were then removed by washing with RPMI-1640. After incubation with RPMI-1640 for 1 day, the stencil was peeled off from the dish, and SECM measurement was performed.

SECM measurements

The measurements were performed in a 4-(2-hydroxyethyl)-1-piperazineethanesulfonic acid (HEPES)-based saline solution (10 mM HEPES, 150 mM NaCl, 4.2 mM KCl, and 11.2 mM glucose; pH 9.5) containing 4.7 mM PAPP and 10% FBS for detecting the ALP-labeled EGFR. ALP catalyzes the hydrolysis of PAPP to yield *p*-aminophenol (PAP) as an enzymatic product, which was detected electrochemically using the microelectrode probe of SECM set at +0.30 V *vs.* Ag/AgCl (Fig. 1a). A disk-type platinum electrode with a 20 μm diameter (Rg 3.0) was used as a SECM microelectrode probe. A fine Pt wire was inserted into a glass capillary, and shielded by thermal fusing of the glass. Finally, the tip of the capillary was carefully polished to give a disk-type microelectrode. Electrochemical current was

measured on the basis of a two-electrode configuration by using an Ag/AgCl electrode as the reference electrode. The details of the SECM system have been reported previously.[8]

Results

SECM imaging of cell patterns

SECM is suitable for noninvasive investigation of the activity of patterned biomolecules. In the past, micro-patterned mammalian cells and enzymes were quantitatively characterized by using SECM.[18,19] Previously, we have shown that EGFR at the cell surfaces can be visualized using ALP as a labeling enzyme. In this study, we used a similar method to investigate the EGFR expression level at the surfaces of CHO, EGFR/CHO, and A431 cells patterned on a solid substrate. EGFR was successively labeled with anti-EGFR and ALP-labeled secondary antibodies. Fig. 2 shows the SECM image of these cells with a line-and-space pattern. The probe electrode of SECM was set at a voltage of +0.30 V and scanned at a distance of 20 μm from the dish to detect the oxidation of the PAP delivered from the labeled ALP. The current responses were based on the electrochemical oxidation of PAP at the SECM probe. Since the ALP labeled on EGFR catalyzes the hydrolysis of PAPP to form PAP, the SECM images can indicate the expression levels of EGFR at the cellular surfaces of 3 different cells. A431 cells showed large current responses, and EGFR/CHO cells showed clear responses, while normal CHO cells showed no obvious signals. This result shows good agreement with the previous results.[8]

Influence of pH on endocytosis

The SECM-based measurement of ALP activity was performed in a relatively high pH solution. A previous study had shown

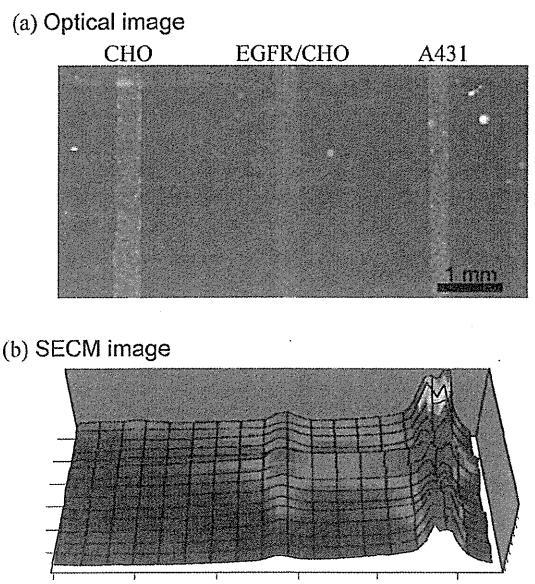

Fig. 2 SECM image of the EGFR expression level of patterned different kinds of cells. (a) Optical microscopy image, (b) SECM image. The electrode was set at 20 μm above the substrate, and the scan rate was 100 μm s^{-1}. The scan range was 7.0 mm × 3.0 mm, and the step size was 100 μm.

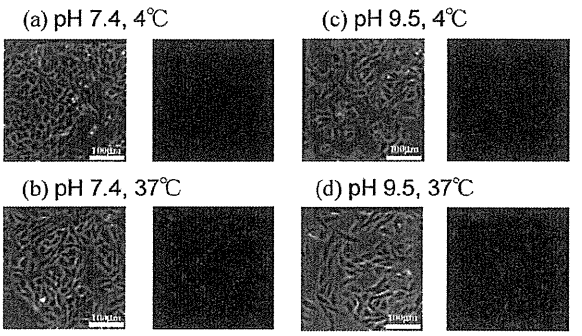

Fig. 3 Investigation of the effect of pH on the EGFR endocytosis. Fluorescent images showed the localization of the EGFR after labelled and stimulated Alexa Fluor® 488 EGF complex. The cells were incubated for 1 hour in phosphate buffer of (a) pH 7.4, 4 °C, (b) pH 7.4, 37 °C, (c) pH 9.5, 4 °C, (d) pH 9.5, 37 °C.

that electrochemical measurement in a solution with pH 9.5 did not cause fatal damage to living cells as long as the measurement period was within several hours.[20] In this study, we investigated the influence of high pH on the endocytosis of living cells by using fluorescent-labeled EGF. The labeled EGF binds to EGFR and triggers endocytosis of the vesicles with EGF–EGFR complexes. Fig. 3 shows the fluorescence images of the cells that were stimulated with EGF and incubated for 1 h in a buffer solution of pH 7.0 or 9.5. When the cells were incubated at 4 °C, clear fluorescence signals were observed on the cell surface [Fig. 3(a) and (c)], indicating that EGFR molecules were present on the cell surface at 4 °C. In contrast, vesicles with high fluorescence intensity were observed inside the cells after incubation for 1 h at 37 °C. Thus, it is obvious that endocytosis does not proceed at 4 °C even in the presence of EGF. Notably, no remarkable differences were observed in the formation of vesicles in the fluorescence images at pH 7.4 and 9.5 [Fig. 3(b) and (d)]. This result indicated that high pH did not influence receptor-mediated endocytosis.

Endocytosis-induced decrease in the EGFR levels at the cell surface

EGF-induced endocytosis promotes changes in the EGFR expression level on the cell surface. This change was measured using fluorescence and electrochemical techniques. In the fluorescence measurements, anti-EGFR IgG labeled with FITC was used to visualize EGFR at the cell surface. In the electrochemical measurements, an ALP-labeled antibody was used to detect EGFR on the cell surface on the basis of electrochemical responses. The cells were incubated with EGF in RPMI-1640 medium for 1 h at 37 °C. After the stimulation with EGF, the EGFR expression levels on the cell surface were detected by fluorescence and electrochemical measurements.

Fig. 4 shows the optical and fluorescence images of EGFR/CHO cells with and without EGF stimulation. Although the EGF-induced change in the cell shape was quite difficult to recognize in the optical image, the fluorescence signal slightly decreased after stimulation with EGF. This decrease was possibly caused by EGF-triggered endocytosis to decrease the levels of EGFR molecules at the cell surface. However,

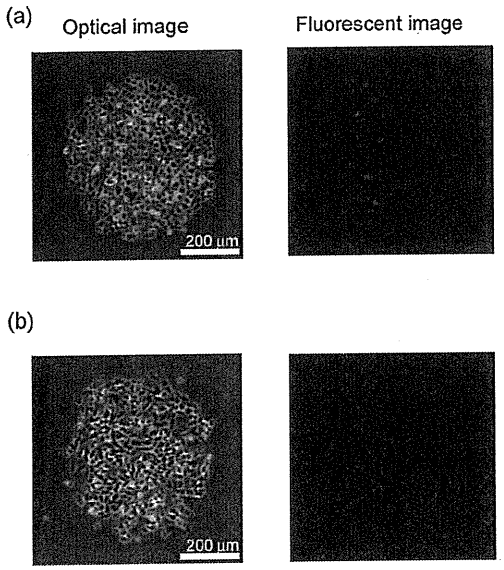

Fig. 4 Investigation of the EGFR expression level of (a) non-stimulated and (b) EGF stimulated EGFR/CHO cells by fluorescent measurement. Fluorescent images showed the expression level of the EGFR. The EGFR was labeled with anti-EGFR IgG FITC conjugated.

although we used confocal microscopy for imaging, it was difficult to discriminate the EGFR on the surface from intracellular EGFR because of the motion of the cellular membrane.

Fig. 5 shows the SECM images of the ALP-antibody-labeled EGFR/CHO cells with and without EGF stimulation together with the corresponding optical images. The labeled ALP catalyzes the hydrolysis of PAPP to yield PAP. The SECM image of cells without the stimulation shows clear responses of the oxidation current at the area of the cell pattern, indicating that SECM can also be used for characterizing the EGFR molecules present on the cell surface. The stimulation with EGF markedly decreased the signal response in the

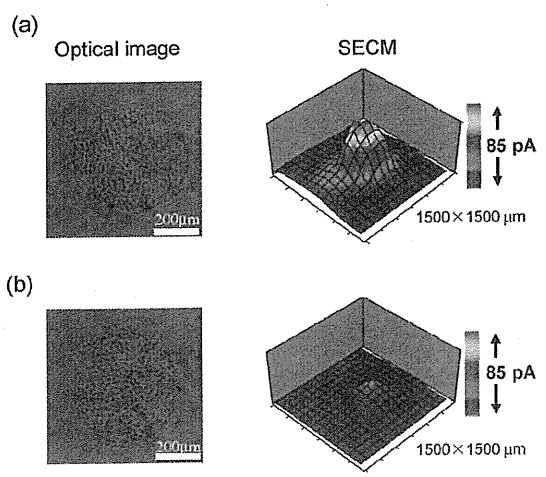

Fig. 5 SECM images of ALP labelled microstencil-patterned EGFR/CHO cells. (a) Non-stimulated and (b) EGF stimulated cells. The electrode was set at 20 μm above the substrate, and the scan rate was 50 m s^{-1}. The scan range was 1500 μm × 1500 μm, and the step size was 50 μm.

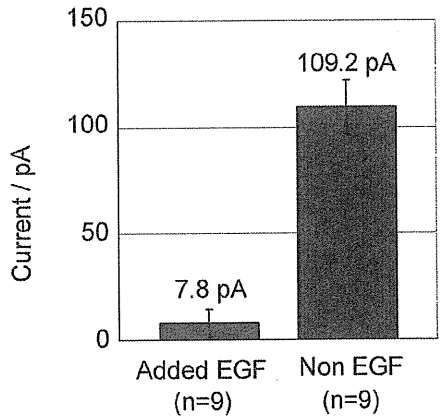

Fig. 6 The current response of EGF stimulated cells and non-stimulated EGFR/CHO cells. The current response was measured by single scan data on the cells pattern.

SECM image. Since the EGFR molecules on the cell surface were detected using SECM, the decrease in the responses indicated the EGF-triggered-endocytosis-induced decrease in the levels of EGFR molecules at the surface. Fig. 6 shows the peak current obtained from the single-scan data on the ALP-antibody-labeled EGFR/CHO cell pattern developed using the previously described procedure.[8] The current responses before and after stimulation with EGF were found to be 109.2 pA and 7.8 pA, respectively. Because of the clear difference in the current responses, we think that SECM measurements are particularly suitable for detecting endocytosis-related events.

Conclusions

In this study, we developed an SECM-based methodology for investigating EGF-triggered endocytosis. This method is suitable for evaluating changes in the EGFR expression level during EGF-triggered endocytosis. SECM enables quantitative evaluation under physiological conditions without having to peel the cells from the culture dish. The current response of the ALP-labeled EGFR/CHO cells investigated using an antibody decreased by 93% after stimulation with EGF. Furthermore, SECM also helped to obtain clear images with adequate spatial and temporal resolutions of the cells before and after occurrence of endocytosis-related events. This methodology is applicable to other biomembrane-related phenomena.

Acknowledgements

This work was partly supported by Grants-in-Aid for Scientific Research (18101006, 21106502, and 22245011) from the Ministry of Education, Culture, Sports, Science and Technology (MEXT), Japan. Y. T. acknowledges support from JSPS Postdoctoral Fellowships for Research Abroad.

Notes and references

1 S. D. Conner and S. L. Schmid, *Nature*, 2003, **422**, 37.
2 K. Roepstorff, L. Grovdal, M. Grandal, M. Lerdrup and B. van Deurs, *Histochem. Cell Biol.*, 2008, **129**, 563.
3 Y. Sako, S. Minoghchi and T. Yanagida, *Nat. Cell Biol.*, 2000, **2**, 168.